Journal of Materials Chemistry A

ARTICLE

Enhancing the oxygen vacancy formation and migration in bulk chromium (III) oxide by alkali metal doping: A change from isotropic to anisotropic oxygen diffusion

Received 00th January 20xx,
Accepted 00th January 20xx

DOI: 10.1039/x0xx00000x

www.rsc.org/

J. J. Carey,[a] and M. Nolan[a]

Oxygen vacancy formation and migration are vital properties for reducible oxides such as TiO_2, CeO_2 and Cr_2O_3 as the oxygen storage capacity (OSC) of these materials are important for a wide range of applications in photovolatics, oxidative catalysis and solid oxide fuel cells. Substitutional doping these transition metal oxides enhances their OSC potential, in particular for oxygenation and surface reaction chemistry. This study uses density functional theory with on-site coloumb interactions (PBE+U) for Cr 3d states (+U=5eV) and O 2p states (+U=5.5eV) to calculate the oxygen vacancy formation energy and oxygen diffusion pathways for alkali metal (Li , K, Na, Rb) doping of bulk chromium (III) oxide (α-Cr_2O_3) . Substitutional doping of the lattice Cr^{3+} cations with alkali metals that have a +1 oxidation state, creates two hole states on the neighbouring lattice O atoms, and removal of a lattice oxygen charge compensates the dopants by filling the holes. The removal of the next oxygen describes the reducibility of doped Cr_2O_3. The oxygen vacancy formation energy is greatly promoted by the alkali dopants with a correlation between the ionic radius of the dopant cation and vacacny formation energy; larger dopants (K, Rb) improve the reducibilty more than the smaller dopants (Li, Na). The activation barriers for oxygen migration along different directions in the alkali metal doped Cr_2O_3 bulk were also calculated to examine the effect of doping on the oxygen migration. The calculated activation energies for the undoped Chromia are symmetric in three dimensions (isotropic) and the presence of the dopants break this isotropy. Alkali dopants promote oxygen migration in the oxygen intra-layers while supressing oxygen migration across the Cr cation layers. The smaller dopants (Li, Na) facilitate easier migration in the oxygen intra-layers to a greater extent than the larger dopants (K, Rb). The Na-Cr_2O_3 bulk promotes both oxygen vacancy formation and migration which makes it a novel candidate for anode materials in medium temperature SOFCs and battery applications.

Introduction

The Chromium oxide is a reducible oxide with a number of oxidation states from Cr(II) to Cr(VI), crystallising in different phases of CrO, Cr_2O_3, Cr_2O_5, and CrO_3, with the hexagonal corundum structure (α-Cr_2O_3) being the most thermodynamically stable at low temperatures and pressures.[1] Chromium (III) oxide (Cr_2O_3) is a dielectric material having a wide band gap (<3eV), and half way between a Mott Insulator and charge transfer semi-conductor,[2, 3] as the valence band maximum (VBM) and conduction band minimum (CBM) are a mixture between Cr 3d states and O 2p states that are characterised by electron-energy-loss spectroscopy,[4] and X-ray photoemission spectroscopy.[5] Density functional theory (DFT) calculations using the generalised gradient approximation (GGA) have calculated the band gap in the range of 2.8eV – 3.1eV, typically underestimated for this method,[6-9] while a screened-exchange hybrid functional method obtained a gap of 3.31eV.[10] Chromia is an anti-ferromagnetic material with alternating "-+-+" Cr layers describing the magnetic ordering throughout the material.[9, 11] Bulk chromia is useful for a wide range of applications in oxygenation catalysis,[12-16] methanol synthesis,[17-19] as an anode material for Li-ion battery applications,[20, 21] in gas sensors,[22] for solid oxide fuel cells,[16, 23] protective coatings,[24, 25] and adhesion promotors.[26] For all these applications the formation of oxygen vacancies and migration throughout the material is crucial to efficiently carry out its role as an active oxidising component.

The oxygen vacancy formation of the bulk α-Cr_2O_3 material can be greatly improved by substitutional doping of the Cr^{3+} cation at its lattice site with a metal dopant to alter the electronic properties of the host material and improve its key properties. This approach is extensively used for improving the oxygen vacancy formation, an important property for redox chemistry and for lattice oxygen mobility, in well-known oxides such as TiO_2,[27-32] and CeO_2.[33-40] Substitutional doping on the host cation site alters the electronic and transport properties, and also the geometry of the material which enhances oxygen vacancy formation and can enhance migration of oxygen throughout the host material (e.g. trivalent doping of CeO_2[37, 40-42]). Doping with a metal that has a lower valence state in its parent oxide than the host oxide material (lower valence dopant, LVD) creates an

[a] Tyndall National Institute, University College Cork, Lee Maltings Complex, Dyke Parade, Cork, Ireland, T12 R5CP

Electronic Supplementary Information (ESI) available: Distribution of oxygen vacancy formation and migration energies in each doped structure. See DOI: 10.1039/x0xx00000x

effective positive charge at the anion lattice site, referred to as a hole state. Dopants with a valence state that is higher in its parent oxide than the host are known as higher valence dopants (HVD) and they introduce excess electrons into the system which typically reduce cations in the host material. Introduction of holes and electrons in such a way through selective doping of materials allows manipulation of the transport properties of the material to improve the key properties, such as nitrogen doping in Cr_2O_3 to improve the mobility of holes for p-type conductivity in the material for optoelectronic devices.[43-46] Mg doping of Cr_2O_3 changes the electronic and local geometric structure of Chromia by replacing a Cr^{3+} cation with an Mg^{2+} cation that creates holes in the material for enhanced p-type conductivity under oxygen rich conditions and this has been extensively studied by experiment and theory.[12, 13, 47-53] Co-doing Cr_2O_3 with both Mg and N shows improved optical and electronic properties over single Mg doped Cr_2O_3;[47, 54] however the Cr_2O_3:N and Cr_2O_3:Mg were found to contain separate phases, and the enhancement was attributed to the Cr_2O_3:N component from the presence of NO^{3-} moieties in the complex, inducing band gap widening that led to improved transmission properties. The growth conditions of Mg:Cr_2O_3 in either Cr-rich/O-poor or Cr-poor/O-rich were found to play a vital role in improving p-type conductivity in Chromia.[53] In the O-rich regime the Mg dopant is uncompensated, displaying p-type behaviour while in the O-poor regime the Mg dopant is likely to be compensated, and filling the holes which is detrimental to p-type conductivity.[55] Experimental studies using X-ray diffraction and X-ray photoemission spectroscopy along with DFT+U calculations showed that co-doping of N and F in Cr_2O_3 greatly distorts the lattice structure however, the N doping was compensated by the F doping and no enhanced conductivity was observed.[52] Doing with Ca,[7] Ti[8] and Fe[56] metal atoms were all found to alter the electronic and magnetic properties of Chromia by reducing the fundamental band gap compared to bulk Chromia, while also increasing the concentration of charge carriers in the material. The aforementioned studies on doping Chromia to alter the fundamental properties of the material for various applications have shown improvement over the bulk undoped material, and such enhancements by substitutional doping are expected to facilitate more facile oxygen vacancy formation and migration in bulk Chromia.

The incorporation of LV metal dopants in bulk metal oxides allows spontaneous formation of oxygen vacancies in the bulk by a charge compensation mechanism, where holes formed after doping are filled with electrons released by the oxygen vacancy to maintain charge neutrality in the bulk material. This is given in Kröger-Vink notation for the example of a +1 metal dopant on a Cr3+ cation site;

$$Cr_{Cr}^{x} + O_{o}^{x} + M_2O \rightarrow M_{Cr}'' + 2O_{\dot{O}} + Cr_2O_3 \qquad \text{(hole formation)}$$

$$M_{Cr}'' + 2O_{\dot{O}} + O_{o}^{x} \rightarrow M_{Cr}'' + 2O_{O}^{x} + V_{o}^{\cdot\cdot} \qquad \text{(compensation)}$$

Where Cr_{Cr}^{x} is a neutral Cr cation on a Cr^{3+} lattice site, M is an LV metal dopant that has an oxidation state of +1, M_{Cr}'' is the metal substituting a Cr^{3+} lattice site with an effective charge of -2, each $O_{\dot{O}}$ is a hole on an oxygen lattice site forming O^{-} (polaron), and $V_{o}^{\cdot\cdot}$ is the formation of an oxygen vacancy at an O^{2-} lattice site with an effective charge of +2 that acts as a charge compensating species. Accounting for charge compensation is critical to correctly describe the ground state electronic structure for modelling and investigating LV dopants in a metal oxide.[33, 34, 36, 37, 39, 55] The resulting reduced bulk oxide is oxygen deficient which can be observed experimentally as the vacancy cannot be annealed in the presence of excess oxygen.[40, 57] These vacancies will therefore always be present in the doped bulk metal oxide creating local distortions in the material allowing improved oxygen vacancy formation and migration throughout the bulk lattice. The removal of a second oxygen species from the bulk lattice is known as the 'active' oxygen vacancy describes the reducibility and the energy required to form this vacancy can be experimentally measured.[57] This approach has been successfully used for +2 dopants in Cr_2O_3,[55, 58] and CeO_2[33, 34, 39] and for +3 dopants in CeO_2[36, 37, 40] and TiO_2[29, 30] where charge compensating mechanisms induce spontaneous oxygen vacancy formation and the active oxygen species is more favourable to form than the oxygen vacancy of the undoped bulk metal oxide.

The diffusion of charge carriers in bulk Cr_2O_3 is important for a number of applications, in particular the movement of oxygen species for anodes in SOFCs, corrosion resistant materials, battery materials and oxygenation catalysis. Not only does the diffusion of defects/ions in the material play a key role in its use for applications, but this is also important for the growth of Cr_2O_3 layers and films. Early Mott-Littleton calculations by Catlow et al.[59] investigated various cation/anion interstitials/vacancies finding that interstitials are favoured over vacancies but the dominant defects are Schottky defects ($2V_{Cr}''' + 3V_{o}^{\cdot\cdot}$) in Cr_2O_3 indicating that vacancy defects are abundant throughout the material into which cations/anions can diffuse, while polarons are the most stable electronic defects that are compensated in the material. Diffusion barriers for the intrinsic defects in bulk Cr_2O_3 were calculated to range from 1.75 – 8.94 eV for cation diffusion and 1.12 – 10.81 eV for anion diffusion depending on the direction of diffusion in the bulk material. DFT+U calculations incorporating the Hubbard +U correction for Cr 3d states have shown that Cr vacancies and Cr Frenkel defects have lower formation energies of 4.84 eV and 2.36 eV, respectively, than oxygen vacancies (5.12 eV) but oxygen diffusion is more facile than Cr diffusion, which is consistent with experimental studies.[6, 60] The calculated diffusion barriers for oxygen migration in the xy-plane (intra-layer) within the same O-layer ranges from 2.21 eV to 3.22 eV, while oxygen migration in the z-direction (inter-layers) across a Cr layer is calculated to range from 2.35 eV to 3.65 eV, showing that migration in bulk Cr_2O_3 is essentially isotropic since the largest barrier is rate determining and is similar in both cases. Classical molecular dynamics simulations also examined point defect migration in bulk Cr_2O_3 for Schottky defect pairs, with oxygen diffusion barriers ranging from 0.57 eV to 1.34 eV at 300 K.[61] Experimental studies have found that oxygen diffusion is

affected by oxygen vacancy formation, and migration becomes more facile along grain boundaries where structural defects and doping in the Cr_2O_3 bulk promote oxygen mobility.[62-64] Although doping has shown to improve the formation of oxygen vacancies in bulk Cr_2O_3 there is no clear indication that doping also improves the diffusion and migration of oxygen throughout the material. To our knowledge, there are no studies that have investigated the effect of doping on the migration of oxygen in bulk Cr_2O_3 and any investigation or knowledge into this area of study is lacking from a computational viewpoint.

Investigations into the formation and migration of oxygen vacancies provide insight into the ability of a metal oxide to diffuse oxygen throughout the lattice which has clear consequences on the oxygenation properties and ionic conductivity of the material for applications in SOFCs and oxygenation catalysis. CeO_2 is known to be an extremely useful reducible oxide material and, the diffusion barrier for oxygen vacancy migration was calculated to be 0.53 eV using DFT+U for a single oxygen migration in the xy plane.[65] The diffusion barrier is concentration sensitive with DFT calculated values varying from 0.46 to 1.08 eV depending on the vacancy concentration in the cell,[66, 67] and biaxial strain on the material was also found to increase the ionic conductivity of the material by reducing the activation energies.[68] Doping CeO_2 with aliovalent metals such as Pr is found to greatly affect the ionic conductivity of the material, with DFT+U calculated activation energies from 0.41 to 0.78 eV depending on the direction of the migration in the bulk.[69] Indeed, doping CeO_2 with lower valence dopants such Nd^{3+}, Y^{3+}, Gd^{3+} is found to greatly improve the ionic conductivity of the material compared to undoped CeO_2, and co-doping combinations with Nd/Y, Nd/Sm, and Pr/Gd are found to further increase the ionic conductivity by up to 40%, presumably in part through a charge compensating mechanism but the authors do not allude to this.[66, 70] Not only does the charge of the dopant have an effect on the oxygen migration energies and mechanism, but also the ionic radius of the dopant incorporated into the lattice. The diffusion of oxygen was examined in Th doped CeO_2 and Ce doped ThO_2 by pair-potential and molecular dynamics calculations. The incorporation of Th in CeO_2 increases the migration barriers, reducing the diffusivity, while incorporation of Ce into ThO_2 decreases the migration barriers, increasing the diffusion of oxygen within the material.[71] The authors find that the mismatch in ionic radius between Ce and Th affects the migration barrier with the dopant having the smaller ionic radius (Ce in ThO_2) increasing the ionic conductivity of the material; however they find that Ce can bind an oxygen vacancy too strongly and under oxygen deficient conditions this can limit the migration of oxygen atoms. This study also compares trivalent and tetravalent dopants, finding that for similar radii cations, trivalent cations bind oxygen vacancies more strongly than tetravalent dopants while tetravalent cations show negative binding energies and trivalent cations show positive binding energies for oxygen vacancies indicating that electrostatics as well as ionic radii play a role in oxygen migration. Although Cr_2O_3 has a larger calculated activation energy barrier for oxygen vacancy migration from DFT+U calculations than CeO_2, it is a more durable, low cost metal oxide material than can withstand higher temperatures and pressures than CeO_2 which make it a more suitable candidate for SOFCs anodes and oxygenation catalysis carried out a temperatures exceeding 1000K. Unlike CeO_2, the oxygen migration process with different dopants has not been studied in Cr_2O_3. We propose that to enhance the oxygen vacancy formation and migration in Cr_2O_3, doping with alkali metals will be a novel approach to realise activation barriers on par with highly reducible metal oxide catalysts such as CeO_2, and allow Cr_2O_3 to be used as a low cost oxide in many applications.

In this study we use DFT calculations with on-site corrected Coulombic interactions (PBE+U) with a Hubbard + U correction applied to the Cr 3d and O 2p states to correctly model the correlated behaviour of α-Cr_2O_3 in investigating the effect of substitutional doping with alkali metals on the oxygen vacancy formation and oxygen diffusion processes. We see that the removal of a first oxygen species from the doped lattice is preferentially next nearest neighbour to the dopant cation in all cases, and the release of two electrons from this process fills the holes on the lattice oxygen atoms generated from the dopant cation (charge compensation). The removal of a second oxygen atom forms the active oxygen vacancy that is of interest for migration. This releases two electrons into the system, reducing neighbouring Cr cations from Cr^{3+} to Cr^{2+}. There is a correlation between oxygen vacancy formation energies and the dopant ionic radius; a larger ionic radius promotes oxygen vacancy formation. Upon doping, the calculated migration barriers do not however, correlate with oxygen vacancy formation energies as the change in structure influences the migration pathways.

Computational Methodology

All calculations are carried out using density functional theory (DFT) within the generalised gradient approximation (GGA)[72] using the Perdew-Burke-Ernzerhof (PBE)[73] exchange-correlation functional as implemented in the Vienna Ab initio Simulation Package (VASP).[74-76] The valence electrons are described using a plane wave basis set and the interaction of the core (Li:[He], Na:[Ne], K:[Ar], Rb:[Kr], Cr:[Ar], O:[He]) and valence (Li $1s^2$ $2s^1$ $2p^0$, Na $3s^1$ $3p^0$, K $3s^2$ $3p^6$ $4s^1$, Rb $4s^2$ $4p^6$ $5s^1$, Cr $3d^5$ $4s^1$, O $2s^2$ $2p^4$) electrons is described using the projector augmented wave method (PAW).[77, 78] The Hubbard +U correction (PBE+U) as described by Dudarev et al.[79, 80] for the electronic on-site coulombic interactions is applied to the Cr 3d (+U=5eV) and O 2p states (+U=5.5eV) which has been shown to correctly described the ground state electronic and magnetic structure of Cr_2O_3 and doped Cr_2O_3.[9, 11, 55] The value of 5.5 eV on the O 2p states has been used in different metal oxides in, e.g. refs. [37],[81] and [38] on CeO2 and TiO2, and in ref. [55] for doped bulk Cr_2O_3. A calculation with this +U correction applied to the free O_2 molecule is required to obtain consistent total energies for the calculation of the O vacancy formation energies throughout the paper. Otherwise the oxygen in the lattice and the oxygen

removed will be described differently and energy differences cannot be computed.

The α-Cr_2O_3 bulk is optimised using a conjugated gradient algorithm at a series of constant volume calculations with the atomic positions and lattice vectors being allowed to relax, where the unit cell lattice constant parameter is varied from ±2% of the experimental value. This was carried out for a number of k-point meshes (4x4x4, 6x6x6, 8x8x8) using the Monkhorst-Pack method,[82] and a number of energy cut-off values (400eV, 500eV, 600eV). The obtained energies for each series of k-point meshes and energy cut-offs were fitted to the Murnaghan equation of state[83] to determine the parameters that provided the lowest energy structure for bulk α-Cr_2O_3. This approach is used to avoid the issues associated with Paluy stress that can occur for plane wave calculations. The optimised parameters for the minimum energy $Cr_{12}O_{18}$ bulk are a k-point mesh of (4x4x4) and an energy cut-off of 500eV, where the lattice constants a=5.08Å, b=4.40Å and c¬=13.93Å deviate from the experimental lattice by 2.48%.[84] The structures were deemed converged when the forces on the atoms were reduced to below 0.02 eV/Å.

To accommodate the inclusion of a dopant species and remove any interactions between images under periodic boundary conditions, the bulk cell for α-Cr_2O_3 was expanded to a 2x2x2 supercell providing a $Cr_{96}O_{144}$ composition with a 1.04% doping concentration for one alkali metal atom on a Cr cation lattice site. This large super cell was relaxed at an energy cut off of 500 eV but with a reduced k-point mesh of (2x2x2). One of the Cr cations was replaced on its lattice site with an alkali metal species (Li, K, Na, Rb), and the system was relaxed. Caesium was also investigated, but convergence could not be achieved. This was attributed to the much larger ionic size of the Cs dopant (1.67Å) compared to Cr cation (0.73Å) which cannot be accommodated in the bulk Cr_2O_3 structure.

The charge compensating oxygen vacancy formation was investigated by exploring the removal of a lattice oxygen species next nearest and next-next nearest neighbour in various sites around the dopant species. The energies for the formation of each compensated vacancy was calculated by;

$$E[comp] = (E[M_x\text{-}Cr_{(2-x)}O_{(3-y)}] + ½\ E[O_2]) – E[M_x\text{-}Cr_{(2-x)}O_3]$$

Where $E[M_x\text{-}Cr_{(2-x)}O_{(3-y)}]$ is the calculated energy for the alkali metal (M) doped bulk α-Cr_2O_3 with the charge compensated oxygen vacancy, $E[O_2]$ is the calculated energy of gaseous O_2 (+U=5.5 eV applied to the O 2p states) and $E[M_x\text{-}Cr_{(2-x)}O_3]$ is the calculated energy for bulk M doped α-Cr_2O_3. This charge compensation mechanism arises because the M^{+1} dopant has a formal oxidation state of two less than Cr^{3+} and will create two holes on neighbouring lattice oxygen atoms. The removal of a lattice oxygen atom will fill the holes with two electrons giving a $[M'_{Cr} + V_{\ddot{O}}]$ ground state. Here we will compare PBE+U and HSE approaches in describing this process as PBE+U can give small positive energies while HSE is known to provide a negative formation energy for lower valence charge compensation in doped oxides.[30] A negative E[comp] indicates that the charge compensation mechanism occurs, and the magnitude of this value is not significant. For the HSE method, 25% Hartree-Fock exchange is used with a screening length of 0.2 $Å^{-1}$. The 'active oxygen vacancy' formation is studied by removing a second oxygen species from the vacancy compensated structure of M doped α-Cr_2O_3. This provides the energy for the active oxygen vacancy formation and is exhaustively explored around the dopant species to obtain the lowest energy position. The energy for the active vacancy for each of the M doped α-Cr_2O_3 is calculated from;

$$E[active] = (E[M_x\text{-}Cr_{(2-x)}O_{(3-2y)}] + ½\ E[O_2]) – E[M_x\text{-}Cr_{(2-x)}O_{(3-y)}]$$

Where $E[M_x\text{-}Cr_{(2-x)}O_{(3-2y)}]$ is the calculated energy for the active vacancy structure, $E[O_2]$ is the calculated total energy for gaseous O_2 as defined above and $E[M_x\text{-}Cr_{(2-x)}O_{(3-y)}]$ is the calculated total energy for the charge compensated structure.

The electronic structure for each of the systems under consideration are examined using the partial (ion and quantum number l decomposed) electronic density of states (PEDOS). The charge interactions and transfer processes are investigated using Bader's atoms in molecules (AIM) approach as implemented in VASP by the Henkleman group,[85-87] and computed spin magnetisations.

The climbing image nudged elastic band approach (CI-NEB) as implemented in VASP by the Henkelman group,[88-90] is used to investigate oxygen vacancy migration in undoped and alkali doped Cr_2O_3. For the undoped Cr_2O_3 bulk, various oxygen vacancy structures are used to anchor the calculation and three 'images' are set up between the start and end points of the calculation. The input 'images' are estimated by generating structures where the migrating oxygen atom to the vacancy site is placed at equidistant positions along a designated migration pathway between two anchor points. The structures are then relaxed with respect to one another using the Broyden-Fletcher-Goldfarb-Shanno algorithm[90] with a similar convergence criteria to the relaxation of the bulk structures. The compensated structures are used as the anchor points for the CI-NEB method to investigate oxygen vacancy migration in the alkali doped Cr_2O_3 structures where the lowest energy structure and the next oxygen lattice position are used as the start and end points of the calculations. The oxygen vacancy migration pathways are explored in between oxygen layers across a Cr cation layer in the z-direction, while intra-layer migration in the xy-plane of the same O layer is also investigated for undoped and doped structures. All TS structures are checked for a single imaginary frequency and relaxing these structures returns to one of the anchor points.

Results

Bulk and Reduced α-Cr_2O_3

The calculated lowest energy structure for bulk α-Cr_2O_3 (Chromia) is shown in Figure 1(a) along with the associated PEDOS. The Cr^{3+} cations adopt distorted octahedral environments in the bulk lattice, while the O^{2-} anions have a tetrahedral geometry. The structure of the bulk Chromia is composed of alternating, neutral stoichiometric Cr_4O_6 layers and the calculated Cr-O bond lengths range from 2.02Å to 2.05Å. The calculated PEDOS plot for bulk Chromia shows that the valence band (VB) and conduction band (CB) are a mixture of Cr 3d and O 2p states. The VB has similar degrees of mixing from the two species while the CB is dominated by Cr 3d states. The calculated band gap between the VB maximum (VBM) and CB minimum (CBM) is 2.60 eV which is underestimated from the experimental value but within the reported range for PBE+U calculations.[6, 53] The calculated Bader charges for Cr^{3+} cations and O^{2-} anions in the Cr_2O_3 lattice are 4.0 e^-, and 7.3 e^-, respectively[55].

To investigate oxygen vacancy formation in the bulk Chromia lattice, an oxygen atom was removed from the lattice and it was allowed to relax with the local geometry around the oxygen vacancy being shown in Figure 1(b) along with the calculated PEDOS plot. The removal of an oxygen atom partially reduces four neighbouring Cr cations as indicated by the orange atoms. As an oxygen vacancy is expected to reduce two Cr cations, various approaches to localise the electrons proved unsuccessful and all structures relaxed to that shown in Figure 1. The complex antiferromagnetic structure with alternating layers may explain the need to move to partial reduction of the Cr to achieve a singlet ground state electronic structure. The PEDOS plot for the reduced Chromia lattice shows the appearance of occupied and unoccupied Cr 3 d peaks in the band gap from the reduction process. The bottom panel of the PEDOS plot shows that the Cr_1 and Cr_2 cations labelled in the local geometry contribute to the spin up Cr 3d states and the Cr_3 and Cr_4 cations contribute to the spin down peak. The occupied and unoccupied Cr peaks in the band gap are located at 0.80 eV and 2.00 eV above the VBM. The calculated formation energy for the oxygen vacancy is 4.11 eV and this is used as a benchmark to examine the removal of oxygen atoms in the alkali metal doped systems.

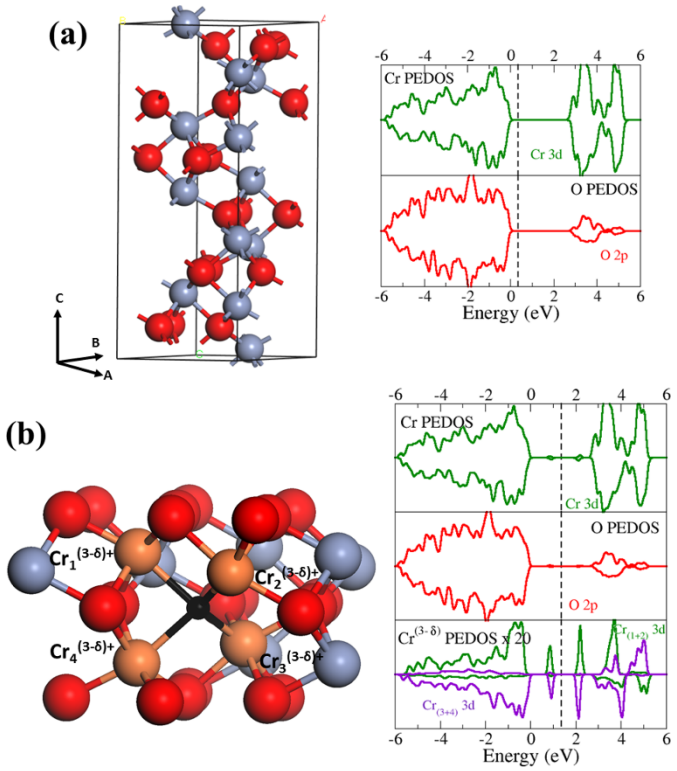

Figure 1: The calculated geometry and PEDOS plots for (a) Bulk α-Cr_2O_3 and (b) reduced α-Cr_2O_3. The unit cell is shown for bulk α-Cr_2O_3 while the local geometry around the oxygen vacancy (black sphere) is shown for the reduced α-Cr_2O_3. The blue, red and orange spheres are the lattice positions of the Cr cations, O anions and reduced Cr cations respectively. The green, red and purple lines are the Cr 3d, O 2p and spin down-$Cr^{(3-\delta)}$ 3d states in the PEDOS plot with the top of the valence aligned to 0 eV and the dotted line showing the position of the Fermi level

Charge compensation and active oxygen vacancy formation in alkali doped α-Cr_2O_3

The doping of bulk Chromia with the alkali earth metals was carried out by replacing a Cr^{3+} cation on its lattice site with an alkali metal (M^{1+}) species. This was carried out for Li, Na, K, and Rb but could not be examined for Cs as already described, arising from the large mismatch in ionic radius with the Cr^{3+} cation. The Cs dopant therefore does not conform to a doping mechanism into the Cr^{3+} lattice site in the bulk, and would either cause a separation of phases between Cr_2O_3 and Cs_2O or remain on the surface of the catalyst. The relaxed local geometries for alkali doped Chromia are shown in Figure 2 along with the calculated PEDOS plots and the dopant oxygen bond lengths are given in Table 1. The substitution of a Cr^{3+} cation with an alkali metal greatly distorts the local geometry with the dopant cation adopting a different geometry to that of the Cr^{3+} octahedral cation. For Li+ the dopant relaxes to a position below the rest of the Cr layer by 0.71 Å to a three coordinated trigonal pyramidal geometry while the larger cations Na^+, K^+ and Rb^+ are all able to maintain the six fold octahedral geometry and move by 0.21 Å, 0.39 Å and 0.33Å below the Cr layer, respectively, giving two sets of M-O distances; three short and three long bonds. The shortest bond lengths in Table 1 are associated with the M-O bonds in the oxygen layer below the dopant cation, while the longest bond lengths are the M-O bonds to the oxygen layer above, with all alkali-oxygen bonds being typical of experimentally determined values in the corresponding bulk oxides.[91]

The introduction of a LV M^+ dopant on a Cr^{3+} cation lattice site is expected to produce two holes on neighbouring oxygen atoms. Examining the Bader values for all oxygen atoms, two oxygen species have a change in Bader value from 7.3 electrons (O^{2-}) to 7.0 electrons (O^-) and have a spin magnetisation value of 0.5, which are thus identified as the hole containing O^- species that are shown in Figure 2 by the light blue spheres. The locations of the O^- species in Li-Cr_2O_3 are both in the upper O layer as low coordinated oxygen atoms above and not coordinated to the Li dopant For Na-Cr_2O_3, K-Cr_2O_3 and Rb-Cr_2O_3

the O^- species are directly coordinated to the dopant in the layers above and below the dopant as shown in the figure.

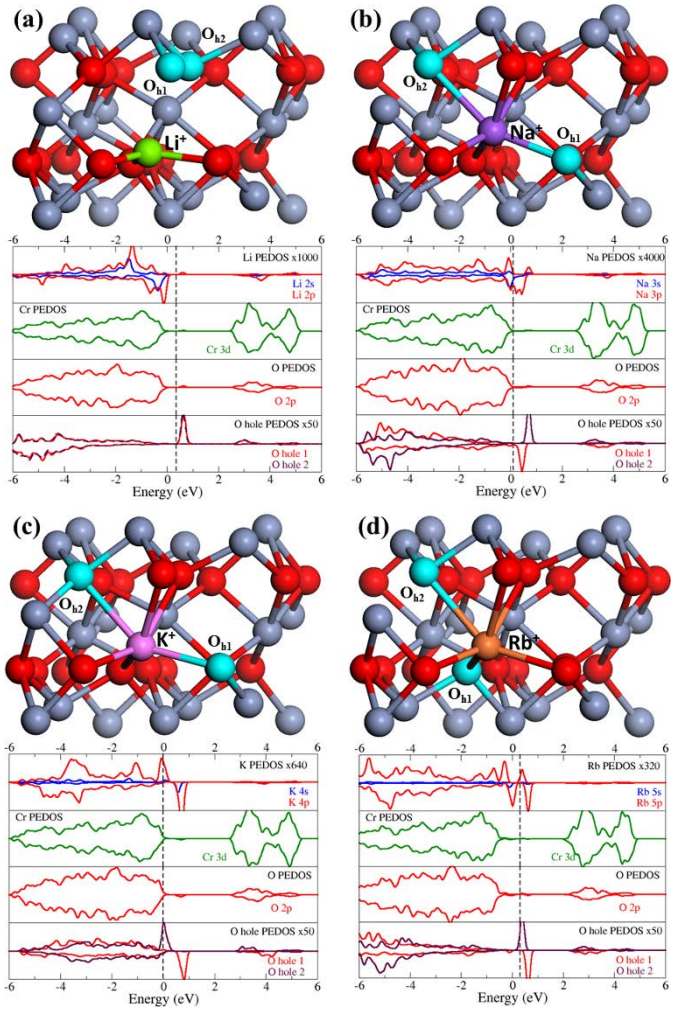

Figure 2: The local optimised geometry and calculated PEDOS for (a) Li-Cr_2O_3, (b) Na-Cr_2O_3, (c) K-Cr_2O_3 and (d) Rb-Cr_2O_3. The grey and red spheres are the lattice positions of the Cr cations and O anions, while the green, purple, pink, and orange spheres show the locations of the Li, Na, K and Rb dopants. The light blue spheres show the locations of the oxygen holes, denoted Oh1 and Oh2. The blue, red, green lines in the PEDOS plot are the s, p and d states with the top of the valence band aligned to 0 eV and the dotted line shows the Fermi level.

The calculated PEDOS plots for each of the doped Chromia systems are shown in the lower panel of Figure 1 below the local structures. The VB and CB are mainly composed of Cr 3d and O 2p states with a minor mixing of alkali Xs/p states (X=2-5) as the concentration of dopant is low. As the energy levels of the dopant increase from 2s/p to 5s/p, the contributions from the dopant to the VB are at a higher energy so that K 4s/p and Rb 5s/p states are located above the Cr 3d and O 2p states. The up shift of the s/p energy states down the alkali group introduces unoccupied metal dopant states above the Fermi level. The lower panel of the PEDOS plots show the contributions from the O^- species as identified by the light blue spheres in the figure, and the O 2p states seen above the Fermi level are unoccupied which are attributed to the hole states on these oxygen atoms. For Li-Cr_2O_3 both O^- species have spin up peaks, while for Na-, K-, and Rb- Cr_2O_3 the oxygen atom in the upper oxygen layer is spin up while oxygen in the lower layer is spin down.

Table 1: The dopant ionic radius and calculated distances for the M - O bonds

Bond	Ionic Radius (Å)	Distance (Å)
Cr – O	0.62	2.05
Li – O	0.59	1.87 (x2), 1.91
Na – O	0.99	2.13 (x2), 2.15, 2.33 (x2), 2.46
K – O	1.38	2.27 (x3), 2.52 (x3)
Rb – O	1.52	2.31 (x3), 2.58 (x3)

The formation of the charge compensating oxygen vacancy in each of the alkali metal doped Chromia structures is investigated by examining the removal of oxygen atoms in next neighbour and next-next neighbour positions in the oxygen layers above and below the dopant cation to identify the position of the lowest energy oxygen vacancy (see supporting information for the range of compensating oxygen vacancies considered). The lowest energy configuration for the charge compensating oxygen vacancies in each alkali doped Cr_2O_3 bulk are shown in Figure 3, along with the corresponding calculated PEDOS plots. The calculated energies for the removal of the charge compensating vacancy are provided in Table 2 for the PBE+U and HSE approaches. The low positive formation energies computed with PBE+U (< 0.71 eV and negative for K^+-doping) and the negative vacancy formation energies for HSE confirm that the removal of the oxygen atom as a charge compensating vacancy is indeed the stable ground state of alkali metal doped Cr_2O_3 as seen previously for doped Cr_2O_3, CeO_2 and TiO_2.[30, 37, 39, 55]

For all alkali doped structures the lowest energy compensating oxygen vacancy is located in the oxygen layer below the dopant cation as indicated by the black sphere in Figure 3. The Li^+ dopant is displaced into the Cr layer above to bond with oxygen in the next anion layer to maintain its three coordinated trigonal pyramidal structure while the Na+ dopant changes to a four-fold square planar geometry to respond to removal of the previously bonded oxygen atom. The larger K^+ and Rb^+ cations cannot exhibit the same flexibility, remaining in similar lattice positions while having a five-fold coordination arising from the removal of the oxygen atoms; their large ionic radii prevents any significant displacement. All bond lengths remain similar to the values given in Table 1. The removal of an oxygen atom releases two electrons to compensate the holes created by the introduction of the alkali metal dopant. The Bader values for the previously identified O^- species in the alkali doped bulk structure, that are shown by the light blue spheres in Figure 2, showing an increase from 7.0 electrons to 7.3 electrons with a spin magnetisation of 0.0. This indicates that the previously formed holes are now filled. This is also reflected in the calculated PEDOS plots in Figure 3, as the lower panel shows that the previously unoccupied states for the oxygen hole are now filled, lying below the Fermi level for all doped alkali metal systems. Further examination of the PEDOS plots show that the

dopant s/p states now have an energy gap between the highest occupied state and the lowest unoccupied state in the overall fundamental band gap of the system.

Table 2: The calculated formation energies for the charge compensating oxygen vacancy in alkali metal doped Cr_2O_3 using the PBE+U and HSE approach

System	PBE+U (eV)	HSE (eV)
Li-Cr_2O_3	+0.71	-2.78
Na-Cr_2O_3	+0.68	-2.49
K-Cr_2O_3	-0.04	-4.51
Rb-Cr_2O_3	+0.13	-3.82

The removal of a second oxygen atom from the alkali metal doped Cr_2O_3 bulk results in the formation of the 'active' oxygen vacancy and the energy associated with formation of this vacancy is a descriptor of the reducibility. In a similar manner to the charge compensating vacancy, oxygen atoms in nearest neighbour and next nearest neighbour positions in the layers above and below the dopant were removed from the compensated structure to identify the lowest energy active oxygen vacancy position in each of the doped structures (the range of energies is given in the supporting information). The lowest energy positions for the 'active' oxygen vacancy in each of the alkali metal doped structures are shown in Figure 4, along with the corresponding PEDOS plots. The active oxygen vacancy is found to be preferentially formed in the oxygen layer nearest neighbour to the alkali metal dopant cation as shown by the dark blue spheres in Figure 4. The formation of a nearest neighbour oxygen vacancy to each of the alkali metal dopants reduces the coordination of the dopant; Li^+ changes coordination to a two-fold bridging cation, Na^+ re-arranges to a four-fold distorted tetrahedral coordination, K^+ adopts a four-fold distorted square planar coordination and Rb^+ has a four-fold distorted tetrahedral geometry. The M-O bond lengths remain similar to those listed in Table 1 and we also note that relaxations around the dopant sites correlate with the dopant ionic radius – the relaxations of neighbouring atoms away from the dopant increase from Li > Na > K > Rb. This is also indicated by the dopant-O bonds in Table 1.

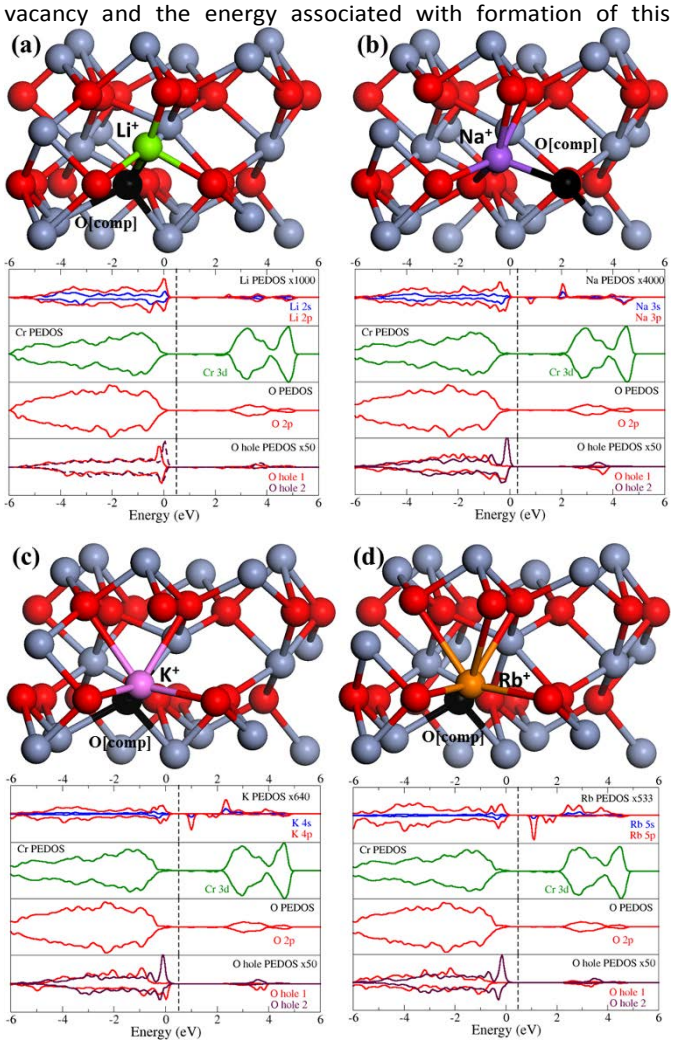

Figure 3: The local optimised geometry and calculated PEDOS for the compensating oxygen vacancy in (a) Li-Cr_2O_3, (b) Na-Cr_2O_3, (c) K-Cr_2O_3 and (d) Rb-Cr_2O_3. The grey and red spheres are the lattice positions of the Cr cations and O anions, while the green, purple, pink, and orange spheres show the locations of the Li, Na, K and Rb dopants. The black sphere shows the location of the most favourable lattice site for the compensated oxygen vacancy. The blue, red, green lines in the PEDOS plot are the s, p and d states with the top of the valence band aligned to 0eV and the dotted line shows the Fermi level.

The calculated PBE+U formation energies for the active oxygen vacancy in each of the alkali metal doped structures are given in Table 3. The presence of the alkali metal greatly decreases the oxygen vacancy formation energy compared to the undoped bulk Chromia (4.11 eV) making it more facile to form oxygen vacancies in the doped bulk. This significant reduction in the formation energy promotes oxygen vacancies in Cr_2O_3, strongly enhancing reducibility. The size of the dopant cation is also seen to play a key role as the formation energy of the active oxygen vacancy decreases further down the group 1 alkali metals which indicates that the large cations allow easier formation of vacancies than the smaller cations. This is due to the release of strain, allowing the larger cation to relax in the off –stoichiometric Cr_2O_3 lattice.

Table 3: The calculated energies for the active oxygen vacancy formation in each of the alkali doped metal structures

System	E[active] (eV)
Cr_2O_3	4.11
Li-Cr_2O_3	2.71
Na-Cr_2O_3	2.27
K-Cr_2O_3	2.14
Rb-Cr_2O_3	1.09

The formation of the active oxygen vacancy in each of the compensated alkali metal doped structures releases two electrons. The extra electrons in the doped bulk lattice are expected to reduce Cr cations and Bader analysis along with spin magnetisation values were used to identify the reduced Cr cations throughout. In all of the doped structures, two Cr cations are reduced from Cr^{3+} to Cr^{2+} and are shown as the green

spheres in Figure 4. These Cr^{2+} cations have an increase in Bader charges from 4.0 electrons (Cr^{3+}) to 4.4 electrons (Cr^{2+}) and have an increase in spin magnetisation from 3.0 to 3.7. The reduced Cr species, denoted as $Cr^{2+}{}_2$, are next neighbour to the active oxygen vacancy and next nearest neighbour to the dopant in Li-Cr_2O_3 and Na-Cr_2O_3, while the opposite is true of the other reduced Cr species, denoted as $Cr^{2+}{}_1$. For K-Cr_2O_3, both reduced Cr^{2+} species are next neighbour to the dopant and active oxygen vacancy as seen in Figure 4(c) and in Rb-Cr_2O_3 both Cr^{2+} species are next-next nearest neighbour to the dopant active oxygen vacancy since the Rb^+ dopant is too large to accommodate the large Cr^{2+} cation (with an ionic radius of 0.80Å) in close proximity.

The PEDOS plots in the lower panel of Figure 4, show that for each of the active vacancies in the doped structures the reduction of the Cr^{3+} to Cr^{2+} cations introduces occupied and unoccupied Cr 3d defect levels in the energy gap between the VB maximum and CB minimum. In each of the doped structures a spin paired solution (singlet) is most stable in which two Cr^{2+} species have opposing α (up) and β (down) spins as indicated in the lower panel of the PEDOS plot. The exception is Rb-Cr_2O_3 where both Cr^{2+} species have α-spins in a triplet configuration which is more stable than a singlet configuration by 0.2 eV. The occupied peak for Li-Cr_2O_3 is located 0.8 eV and the unoccupied peak is located at 2.0 eV above the top of the VB. For Na-Cr_2O_3 these peaks are located at similar energies to Li doped Chromia. In K-Cr_2O_3, the β-spin occupied peak is at 0.52 eV and the α-spin occupied peak is located at 0.82 eV above the top of the VB. The unoccupied Cr 3d peaks start at 1.12 eV above the top of the VB. For Rb-Cr_2O_3, the Cr 3d peaks from the reduced cations are located around 0.39 eV and an unoccupied Cr 3d peak is located at 1.02 eV above the VBM.

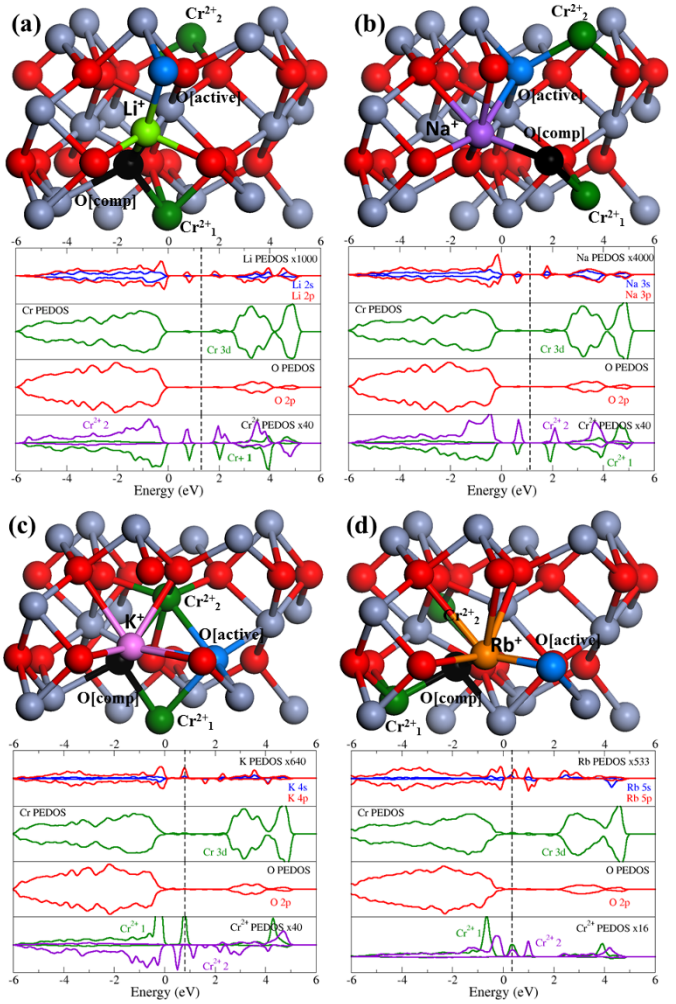

Figure 4: The local optimised geometry and calculated PEDOS for the active oxygen vacancy in (a) Li-Cr_2O_3, (b) Na-Cr_2O_3, (c) K-Cr_2O_3 and (d) Rb-Cr_2O_3. The grey and red spheres are the lattice positions of the Cr cations and O anions, while the green, purple, pink, and orange spheres show the locations of the Li, Na, K and Rb dopants. The black sphere shows the location of the most favourable lattice site for the compensated oxygen vacancy, while the dark blue sphere shows the location of the active oxygen vacancy. The Cr^{2+} cations are shown by the dark green spheres. The blue, red, green lines in the PEDOS plot are the s, p and d states with the top of the valence band aligned to 0eV and the dotted line shows the Fermi level.

Migration of oxygen vacancies in undoped Cr_2O_3

The oxygen vacancy migration barriers were calculated along the [010], [100] and [110] -directions for the undoped Cr_2O_3 bulk as a reference to compare with computed migration barriers in the alkali metal doped Cr_2O_3 bulk structures. The [010], [100] and [110] direction are considered for oxygen migration along the *x*, *y* and *z* coordinates, respectively. The

structures for the starting and end points of the calculations with the optimised transition states (TS) along the pathways are shown for the [010] and [100] directions in Figures 5(a) and (b), respectively, and for the [110] direction in Figure 6. There are a larger number of images calculated for migration in the [110] direction than for the [010] and [100] directions as the environment of the oxygen atoms is asymmetric along the [110] migration pathway. The coordination within the layers is symmetric along the migration pathway. This results in two TS state structures for the [110] direction. In each of the figures, the black sphere shows the location of the vacancy and the yellow sphere shows the lattice oxygen atom that is migrating between the vacancies. The calculated minimum energy pathways and activation barriers along each migration direction are shown in Figures 7(a)-(c), with each of the points on the energy curve corresponding to an image of the CI-NEB calculation and the TS energy labelled for the structures in Figures 5 and 6. The plots shown in Figure 7 are determined by using the total energy with the active oxygen vacancy as the reference point denoted E[Ovac], and plotting the energy for each of the images with respect to this energy as E[image] - E[Ovac]. The energy difference is then plotted against the change of coordinate for the migrating oxygen atom along each migration direction. For the [010] direction in Figure 5(a), the migrating oxygen changes from a tetrahedral coordination with four Cr-O bonds (2.02-2.06Å) to a two-fold bent coordination in the TS with two Cr-O bonds (2.36Å, 1.36Å) with a calculated activation energy of 3.30 eV. The calculated TS for the [100] direction shown in Figure 5(b) has a similar geometry to the [010] direction; the migrating oxygen atom changes from the tetrahedral coordination to the two fold bent configuration (Cr-O bonds: 2.08Å, 1.83Å). The calculated activation energy for the [100] direction is 3.30 eV, which is the same as the [010] direction, and both are activation energies similar to previous studies.[6] The [010] and [100] directions having similar structures and energies indicates that oxygen vacancy migration can proceed in either direction within a layer once the system has enough energy to overcome the high activation barriers.

The calculated structures along the oxygen vacancy migration path in the [110] direction (Figure 6) show that initially the migrating oxygen atom changes coordination from a four-fold tetrahedral to a two-fold bent geometry (Cr-O: 1.90Å, 2.18Å) by breaking one of the Cr-O bonds as shown in Figure 6(ii), which is the TS structure for oxygen migration (Figure 7(c)(ii)). The calculated activation energy to overcome this transition state is 2.54 eV. The migrating oxygen maintains this geometry in the second TS (Figure 6(iii)) with distances of Cr-O 1.78Å (x2), and a calculated activation energy of 3.30 eV; this is similar to the

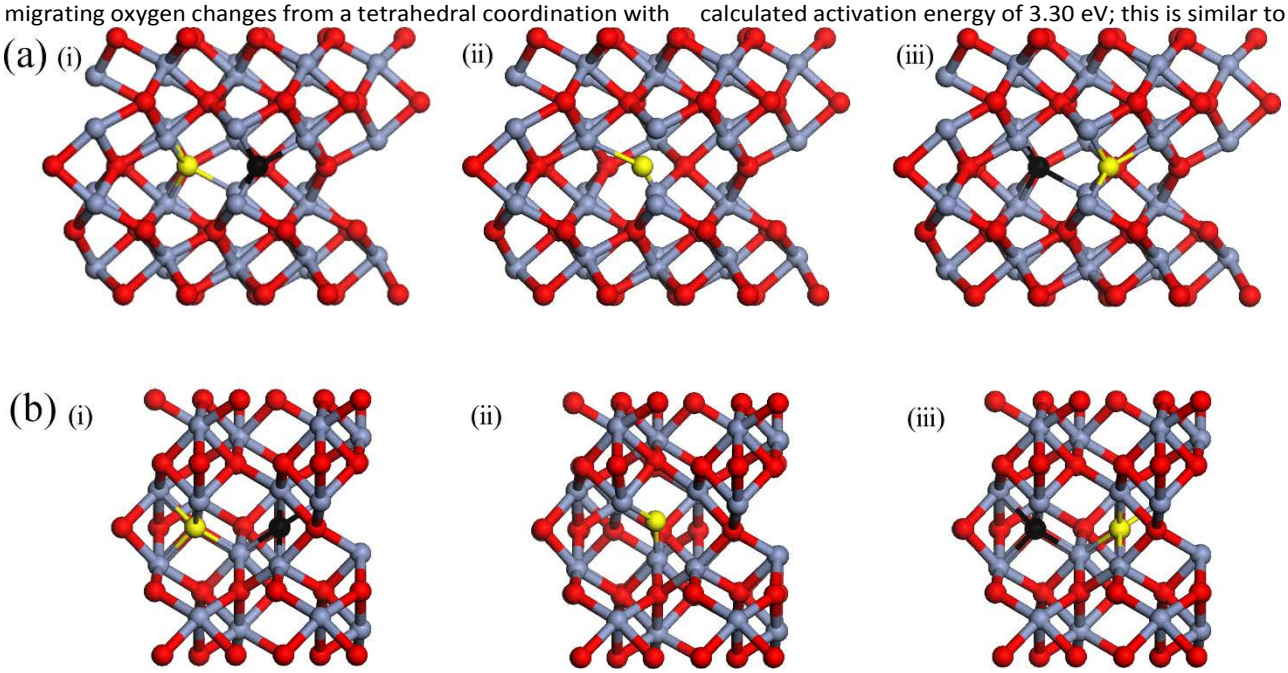

Figure 5: The migration of oxygen in the (a) [010] direction and (b) the [100] direction. The starting point for each calculation is shown in (i), along with (ii) the calculated transition state and (iii) the end point of the calculation. The grey and red spheres are the lattice positions of the Cr^{3+} and O^{2-} ions, while the yellow sphere shows the migrating oxygen atom and the black sphere shows the lattice oxygen vacancy positon.

activation energies in the [010] and [100] directions. The difference in energy barriers for migration along the [110] direction can be attributed to the first TS requiring the breaking of only one Cr-O bond, while the second TS has an additional energy cost to break two Cr-O bonds before changing to the final tetrahedral configuration. The energy barrier of 2.54 eV across the first Cr layer is lower than the [010] and [100] directions implying that oxygen migration in the inter-layer [110] direction across the Cr layer is more facile than in the intra-layer {100} plane (inclusive of symmetrically equivalent [010] and [100] directions); however, as the activation energy across the second Cr-layer is similar to the energies calculated for the {100} plane, any oxygen atoms migrating across the first layer will be limited by the energy required to migrate through the second Cr-layer. This would be the rate limiting energy barrier and it being similar to the {100} plane would imply that

reaching this energy barrier would also allow diffusion in the {100} plane, suggesting that migration in all three directions is possible by overcoming this energy barrier of 3.30 eV. This is of course significantly higher than in other metal oxides such as CeO_2, and we now discuss the effect of alkali metal doping on these migration barriers.

Migration Barriers for [010] direction in Alkali doped Cr_2O_3

The oxygen migration barriers for alkali metal doped Chromia are calculated in a similar manner to the undoped Chromia bulk with multiple images used in the calculation constructing a similar energy profile to that shown in Figure 7. The most stable vacancy structure (active oxygen vacancy) in each doped structure (Figure 4) is used as the starting point, with the neighbouring oxygen and next neighbouring oxygen vacancy sites used as the end points of each CI-NEB calculation. As the distribution of oxygen vacancy sites is no longer symmetric compared to undoped Chromia bulk, the energy profiles and migration barriers are asymmetric. The [010], [100] and [110] directions are considered for oxygen migration along the *x*, *y* and *z* coordinate. Multiple migration pathways are examined to investigate barriers close to the dopant species (neighbouring oxygen atom) and further away from the dopant (next-neighbouring oxygen) in the bulk lattice, resulting in multiple transition state (TS) structures. This will provide evidence if the oxygen migration is affected in a local or non-local manner by the presence of the dopant in the bulk lattice.

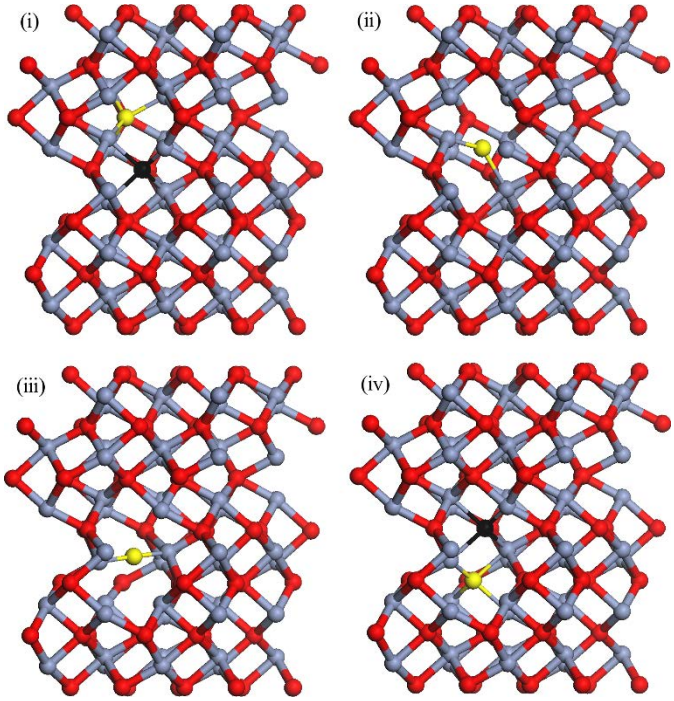

The calculated TS structures and the corresponding activation energies for the alkali doped bulk Chromia along the [010] direction are shown for each dopant in Figure 8(a)-(d); the end points for the CI-NEB calculation are indicated by (i) and (iv). The full energy profile including all images (similar to Figure 7) for the migrating oxygen species are shown in the supporting information and for this discussion it is sufficient to present the activation energies (Figure 8). The two transition state structures can be described as one being next nearest neighbour from the dopant cation (TS-1) while the second transition state (TS-2) is nearest neighbour to the dopant cation. For Li-Cr_2O_3 migration of oxygen along the [010] direction starts from a next nearest neighbour position and the structure for the first TS (TS-1) (Figure 8(a)(ii)) has the migrating oxygen coordinated to two Cr cations (Cr-O: 1.83Å, 2.08Å), while the migrating oxygen in the second TS structure (TS-2) where O coordinates to the Li dopant takes a three-fold planar geometry with two Cr-O bonds (2.19Å, 1.88Å) and one Li-O bond (1.93Å). The calculated activation energies for both TS structures are similar (+1.54eV and +1.59eV) indicating that migration in the [010] direction is substantially lowered compared to bulk Chromia. Starting from migration of O initially next nearest neighbour to Na (Figure 8(b)(ii)) and K (Figure 8(c)(ii)), in TS-1 the migrating oxygen has a similar two-fold bridging geometry to that seen for Li-Cr_2O_3 with two Cr-O bonds of 2.07Å (1.96Å) and 1.83Å (1.82Å) in Na-Cr_2O_3 (K-Cr_2O_3). The calculated activation energy for TS-1 is +2.83eV and +3.04eV in Na-Cr_2O_3

Figure 6: The migration of oxygen in the [110] direction. The starting point for the calculation is shown in (i), along with the transition states (ii) – (iii) and the end point of the calculation is (iv). The grey and red spheres are the lattice positions of the Cr^{3+} and O^{2-} ions, while the yellow sphere shows the migrating oxygen atom and the black sphere shows the lattice oxygen vacancy positon

and K-Cr_2O_3, respectively, indicating that the activation energy for O migration increases with increasing ionic radius of the dopant cation from Li to K for the next nearest neighbour oxygen migration; however, in all cases it is still reduced compared to migration in bulk Chromia.

The structure for TS-2 state, in which oxygen coordinates to the dopant cation has a trigonal planar geometry for Na-Cr_2O_3, with

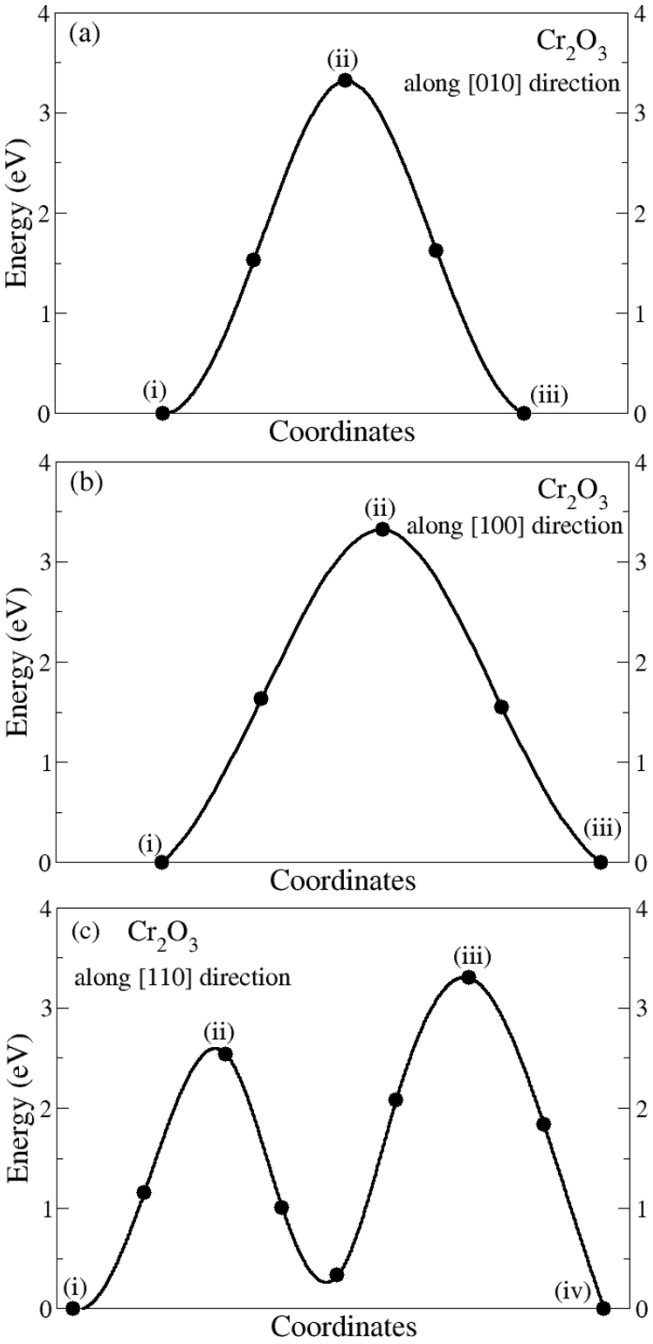

Figure 7: The calculated energy barriers in undoped Cr_2O_3 along the (a) x-direction, (b) y-direction and (c) the z-direction. The numbers (i) - (ix) along the curves correspond to the images in Figure 5 and 6.

Cr-O bond lengths of 2.00Å, 1.88Å, and a Na-O bond length of 2.23Å. In K-Cr_2O_3 TS-2 structure has a two-fold bridging oxygen with Cr-O bond lengths of 2.14Å and 1.93Å, and the K-O distance is 3.17Å. The calculated activation energy for TS-2 is +1.47eV and +1.31eV in Na-Cr_2O_3 and K-Cr_2O_3, respectively, indicating the activation energy close to the dopant cation decreases with increasing ionic radius which is the opposite trend to the next nearest neighbour transition state.

Figure 8: The calculated CI-NEB pathway for oxygen migration along the [010] direction in (a) Li, (b) Na, (c) K and (d) Rb doped Cr_2O_3 showing the (i) the starting point, (ii) TS-1, (iii) TS-2 and (iv) the end point along with the activation energy for each TS. The grey and red spheres are the lattice positions for the Cr cations and O anions, while the green, purple, pink and orange spheres are the Li, Na, K, and Rb dopants respectively. The migrating oxygen species is shown by the yellow sphere in each image.

Journal of Materials Chemistry A

ARTICLE

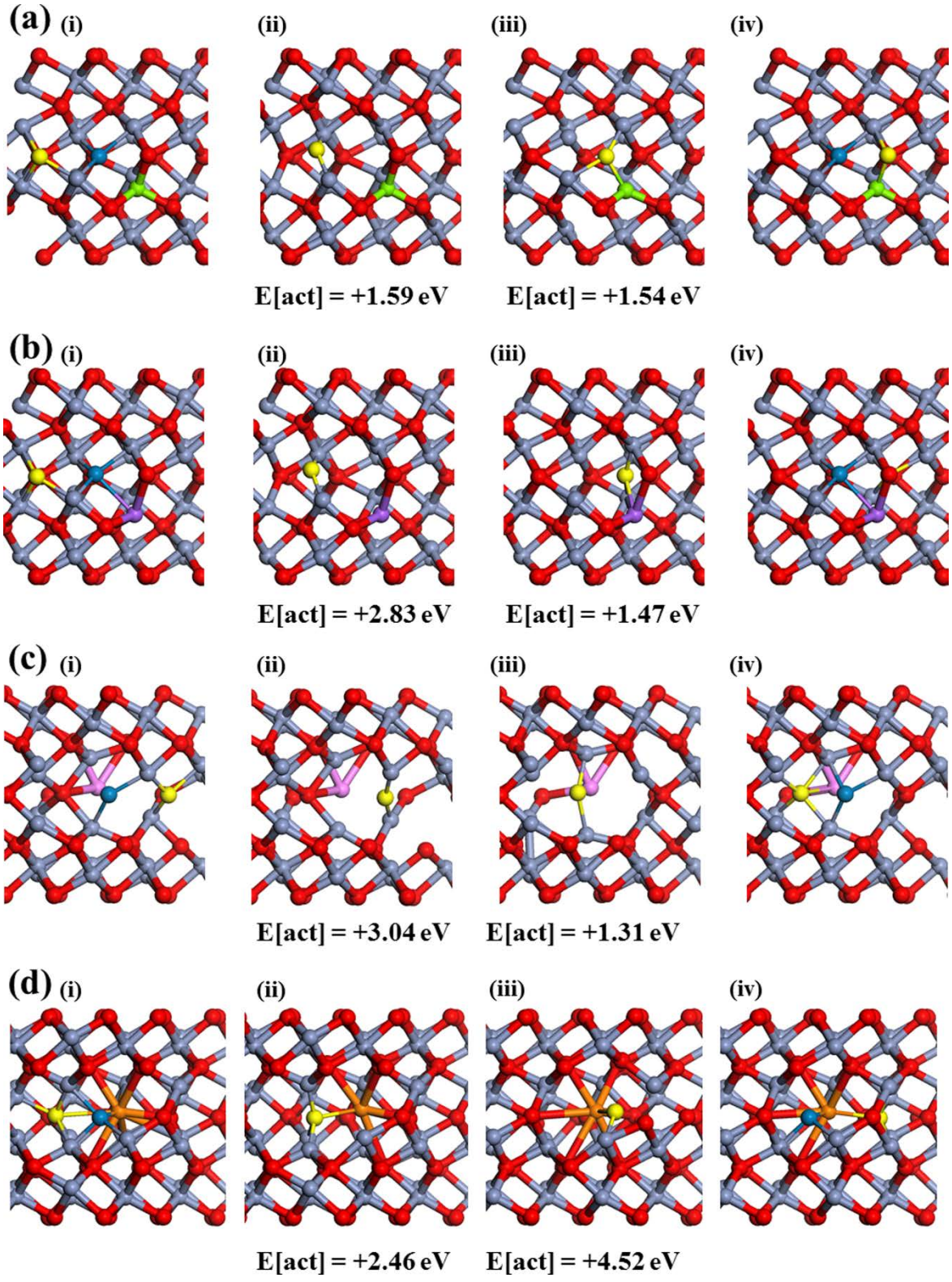

In Rb-Cr_2O_3, the much larger cation size compared to the other dopants has a profound effect on the migration barrier and TS. The TS-1 structure has a tetrahedral geometry with three Cr-O bonds (1.89Å x2, 2.11Å) and an Rb-O bond length of 2.45Å, while the TS-2 structure close to the Rb dopant has a two-fold bridging geometry with a Cr-O (1.93Å) and Rb-O (2.31Å) bonds. The calculated energy for the migration of oxygen from the next nearest neighbour position is +2.46eV which is lower than the corresponding TS in K-Cr_2O_3 and Na-Cr_2O_3 as the larger size of the Rb dopant allows Rb-O bonding to stabilise TS-1. However, for TS-2 close to the Rb cation, the calculated activation energy of +4.52eV is much larger than even undoped Cr_2O_3 and does not follow the trend of the other dopants. The large size of the Rb dopant makes the migration near the dopant more difficult, most likely arising from the inability of the large Rb cation to move. In contrast the smaller dopants can accommodate movement of oxygen past the dopant. The large ionic radius of Rb therefore promotes oxygen migration away from it while hinders nearby migration.

Migration Barriers for [100] direction in Alkali doped Cr_2O_3

The calculated TS structures and corresponding activation energies for the oxygen migration along the [100] direction (change in y coordinate) are shown in Figure 9(a)-(d); the end points for the CI-NEB calculation are parts (i) and (iv). Along the [100] direction, oxygen migrates across the dopant cation in TS-1. In the TS-2 structure, oxygen migration is next nearest neighbour to the dopant species. For Li-Cr_2O_3 and Na-Cr_2O_3 in the TS-1 structure, the migrating oxygen takes three-fold trigonal planar geometry with two Cr-O bond lengths of 1.87Å (1.87Å), and 2.11Å (1.98Å) in Li-Cr_2O_3 (Na-Cr_2O_3), and a Li-O (Na-O) bond length of 1.95Å (2.18Å). The structure for TS-1 in K-Cr_2O_3 has a two-fold bridging coordination with Cr-O and K-O bonds that are 1.74Å and 2.32Å. The calculated activation barriers for the oxygen migration across the dopant cation increase from 1.57eV to 3.65eV with increasing dopant ionic radius from Li to K. Unlike the [010] direction, the migration across the dopant cation in the [100] direction is gradually hindered by the increasing size of the dopant ionic radius as the hexagonal structure of the bulk Chromia is shorter in this direction and cannot accommodate the migration in a similar way to the [010] direction.

In the TS-2 structure, oxygen takes a two-fold bridging coordination for Li-, Na-, and K-, doped Cr_2O_3. All three structures having similar Cr-O bond lengths of 1.84Å and 2.11Å. The calculated activation energies for oxygen migration next nearest neighbour to the dopant are similar for Li and K doped Cr_2O_3 while Na-Cr_2O_3 has a lower activation energy. However, these only show a small decrease compared to undoped Cr_2O_3. For Li and Na doped Cr_2O_3, the activation energy away from the dopant has a higher energy than across the dopant suggesting that the dopant facilitates oxygen migration in the [100] direction, while for the larger ionic radius of the K dopant the oxygen migration is impeded with a larger activation energy than the undoped Chromia system. Similar to the [010] direction, the oxygen migration for the Rb-Cr_2O_3 does not follow the same trend as the other dopants. The TS-1 structure, with oxygen closest to the Rb dopant (Figure 9(d) (ii)), has a two-fold bridging oxygen with Cr-O and Rb-O bond lengths of 1.74Å and 2.42Å. The TS-2 structure for the next nearest neighbour oxygen site (Figure 9(d) (iii)) is also two-fold bridging with two Cr-O bonds (1.82Å, 2.07Å). The calculated activation energy for the TS-1 across the Rb dopant (+3.30eV) shows no improvement over the undoped Cr_2O_3 lattice, while the nearest neighbour oxygen migration away from the Rb dopant has a similar energy to Li-Cr_2O_3 and K-Cr_2O_3 but the change is minimal compared to the undoped Chromia system.

Migration Barriers for [110] direction in Alkali doped Cr_2O_3

The calculated TS structures and corresponding activation energies for the alkali doped bulk Chromia along the [110] direction (change in z coordinate) are shown in Figure 10(a)-(d); the end points for the CI-NEB calculation are parts (i) and (iv). As the *c*-vector for bulk chromia is longer than the *a* and *b* vectors, a larger number of images are required to provide sufficient sampling along the [110] direction, resulting in the three TS structures shown in Figure 10. Unlike the oxygen migration in the intra {100} planes of the layers, there appears to be no observable trend down the alkali dopants for the interlayer oxygen migration along the [110] direction.

For Li-Cr_2O_3, each of the TS structures are similar having a two-fold bridging geometry with Cr-O bond lengths of 2.27Å, and 1.90Å in TS-1 (Figure 10(a)(ii)), 1.80Å in TS-2 where oxygen migrates across the Li dopant with a Li-O bond length of 1.79Å (Figure 10(a)(iii)), and in TS-3 (Figure 10(a)(iv)) with two Cr-O and Li-O bond lengths of 1.87Å, 2.43Å and 2.21Å. The calculated activation energies for the TS structures in Li-Cr_2O_3 indicate that the activation energy for oxygen migration increases as oxygen moves past the dopant while this is lower for next nearest neighbour oxygen migration towards and away from the Li dopant.

Journal of Materials Chemistry A

ARTICLE

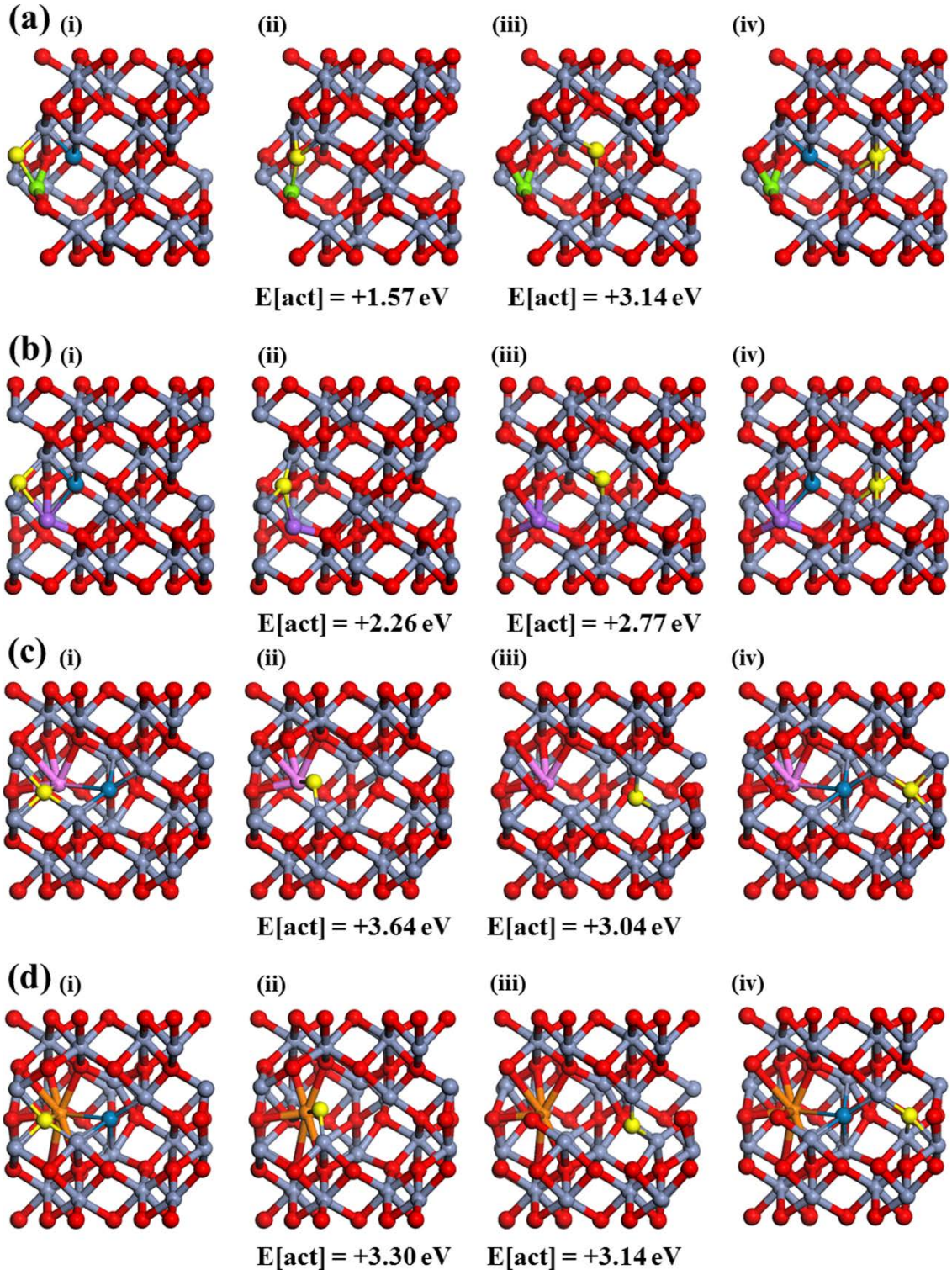

Figure 9: The calculated CI-NEB pathway for oxygen migration along the [100] direction in (a) Li, (b) Na, (c) K and (d) Rb doped Cr_2O_3 showing the (i) the starting point, (ii) TS-1, (iii) TS-2 and (iv) the end point along with the activation energy for each TS. The grey and red spheres are the lattice positions for the Cr cations and O anions, while the green, purple, pink and orange spheres are the Li, Na, K, and Rb dopants respectively. The migrating oxygen species is shown by the yellow sphere in each image.

Journal of Materials Chemistry A

ARTICLE

The coordination geometries for each of the TS structures in Na-Cr_2O_3 are similar these for Li-Cr_2O_3 with Cr-O bond lengths of 1.79Å (x2) in TS-1. In TS-2 the Cr-O and Na-O bond lengths are 1.78Å and 2.05Å. Finally the structure for TS 3 has Cr-O and Na-O bond lengths of 1.85Å and 2.16Å. Similar to the Li-Cr_2O_3, the largest calculated activation barrier for oxygen migration is found when the oxygen is migrating past the Na dopant, with smaller (but still similar to undoped Cr_2O_3) activation energies calculated for migration to next nearest neighbour positions away from the Na dopant; all activation energies are larger than calculated for Li-Cr_2O_3. The largest activation energies for both dopants are larger than for undoped Chromia (+3.30eV) so that the presence of the Li and Na dopants will not promote oxygen migration in the [110] direction. The oxygen migration along the [110] direction for Rb-Cr_2O_3 is similar to Li and Na doped Cr_2O_3 as the coordination geometry of the TS structures are similar and the calculated activation energies show similar behaviour with the largest activation energy for oxygen migration being closest to the Rb dopant (+4.34eV) and smaller activation energies for the next nearest neighbour oxygen migration away from the Rb dopant similar to Li-Cr_2O_3 and Na-Cr_2O_3.

The oxygen migration process in the [110] direction for K-Cr_2O_3 shows different behaviour to the other alkali dopants. Although the TS structures have similar two-fold bridging geometries to the other dopants, the lowest calculated activation energy barrier is when oxygen neighbours the K dopant and the activation barriers are larger for oxygen migration to next nearest neighbour positions, unlike Li, Na and Rb doped Cr_2O_3. The lower activation energy when oxygen neighbours the K dopant is due to the position of the charge compensating vacancy which provides space to reduce the strain around the K dopant, facilitating more facile oxygen migration close to the K dopant. If charge compensation was not considered, this property of K doping would not have been observed, providing further evidence to the importance of considering charge compensation in doped metal oxide systems.

Discussion:

The results of this work show that substitutional doping of alkali metals in Chromia creates hole states on neighbouring oxygen species that are charge compensated by spontaneous formation of oxygen vacancies. The formation of an active oxygen vacancy acts as a descriptor for reducibility. The introduction of the alkali dopants greatly promotes the reducibility of Chromia by decreasing the computed oxygen vacancy energy from 4.11 eV (undoped) to 2.71eV for Li-Cr_2O_3, 2.27eV for Na-Cr_2O_3, 2.14eV for K-Cr_2O_3 and 1.09eV for Rb-Cr_2O_3. There is a correlation between the ionic radius and the oxygen vacancy formation energies down the group 1 metals as shown in Figure 11; albeit not a perfect linear correlation. As the metal dopant gets larger the reducibility of the Chromia lattice increases. This indicates that larger dopant cations in Chromia decrease the oxygen vacancy energy and promote reducibility in the material. Such correlation between oxygen vacancy formation and dopant ionic radius has been seen for alkaline earth metals in CeO_2.[34] This can be generally attributed to the distortions induced by the presence of the dopant on the host lattice site which has a different ionic radius, different preferred coordination environment and (possibly) different oxidation state. The effect of dopant ionic radius on the reducibility of CeO_2 with Th and U dopants, as well as Ce doping in ThO_2 and UO_2 also has an effect on oxygen vacancy migration in these metal oxide materials which impacts on their properties for various oxygen mediated catalysis and applications.[71]

Although oxygen vacancy formation energy is a strong indicator for the reducibility of the material, it cannot be a descriptor for the mobility of oxygen vacancies through the material. The investigation of oxygen migration in alkali metal doped bulk chromia in this study shows that oxygen migration is a complicated process with the presence of the dopant significantly altering the migration pathways in bulk Chromia along the [010], [100] and [110] directions. From the calculated activation energies of the transition states in each doped structure, the highest energy and rate limiting barriers in each direction are summarised in Table 4. These energies are important as they will control the oxygen migration in the alkali metal doped bulk Chromia. For Li, Na and Rb dopants, the activation barriers in the [110] direction are larger than the undoped bulk indicating that the presence of the dopants supresses inter-layer oxygen migration, while K doping shows a negligible improvement over undoped Chromia. The Li-Cr_2O_3 and Na-Cr_2O_3 doping promote intra-layer oxygen migration in the {100} planes ([010] and [100] directions) in particular for the [010] direction in Li-Cr_2O_3 which can explain its usefulness as a cathode material in SOFCs and Li-ion batteries that is worthy of further study.[20, 21]

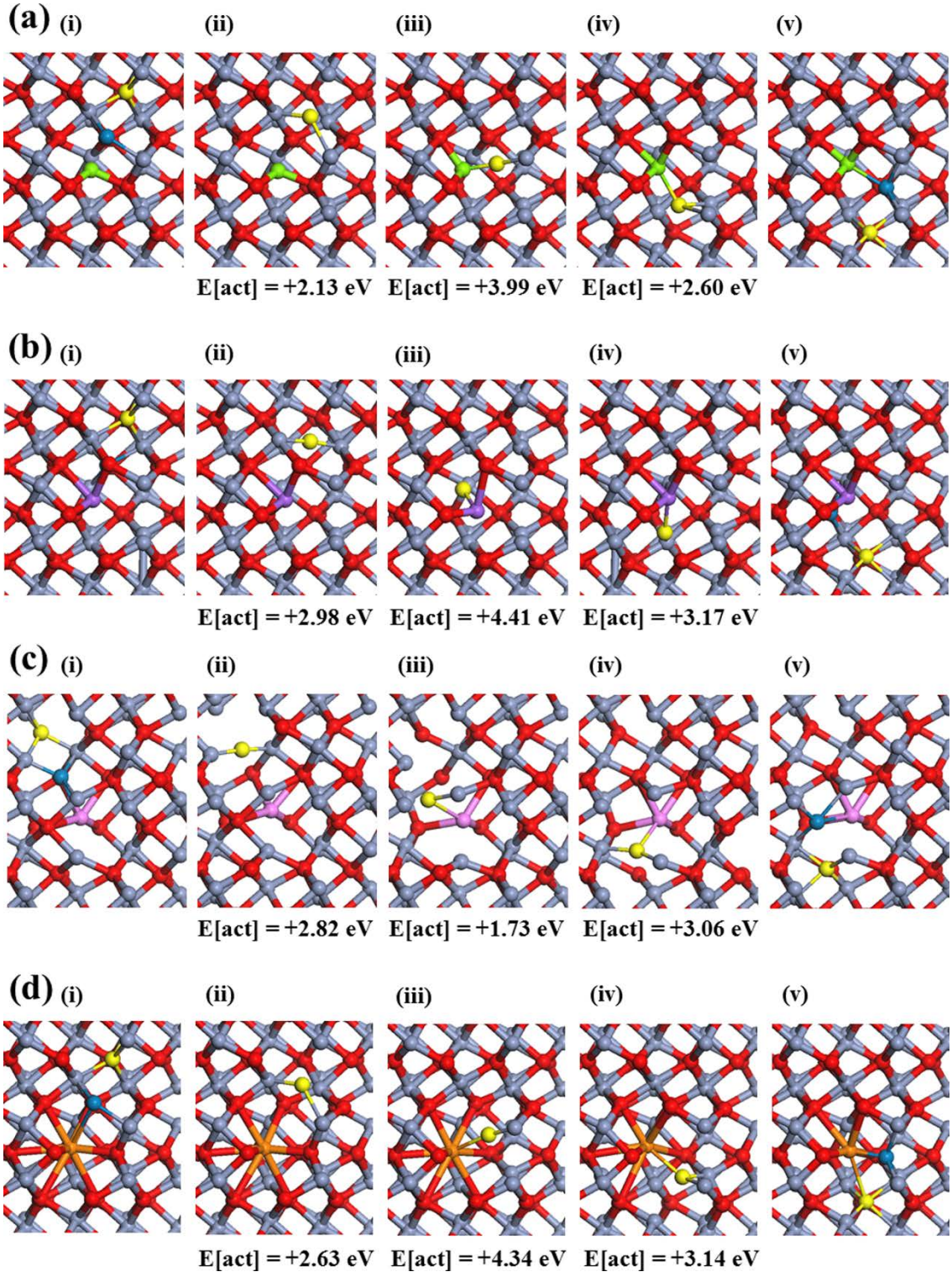

Figure 10: The calculated CI-NEB pathway for oxygen migration along the [110] direction in (a) Li, (b) Na, (c) K and (d) Rb doped Cr_2O_3 showing the (i) the starting point, (ii) TS-1, (iii) TS-2, (iv) TS-3 and (v) the end point along with the activation energy for each TS. The grey and red spheres are the lattice positions for the Cr cations and O anions, while the green, purple, pink and orange spheres are the Li, Na, K, and Rb dopants respectively. The migrating oxygen species is shown by the yellow sphere in each image.

Journal of Materials Chemistry A

ARTICLE

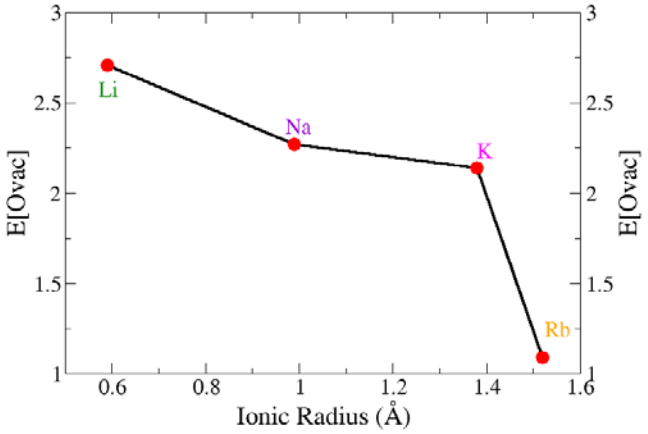

Figure 11: The plot of oxygen vacancy formation energy with respect to dopant ionic radius in each of the alkali metal doped Chromia bulks.

The K-Cr_2O_3 system also shows a slight improvement for the oxygen migration in the [010] direction but has a larger activation energy in the [100] direction than the undoped bulk. Rb-Cr_2O_3 does not promote oxygen migration in any direction of the bulk lattice as the large ionic radius of the Rb limits the oxygen migration pathways. This too can be said for K doping as the improvement of the activation energies over the undoped bulk is not as significant as either Li-Cr_2O_3 or Na-Cr_2O_3. However, examining the activation barriers for K doping, the lowest energy barriers are where the migration is closest to the K dopant in each direction. This is facilitated by the position of the charge compensating oxygen vacancy which indicates that a local improvement is possible for K doping. A larger concentration of K doping may improve the oxygen migration in the bulk Chromia due to this localised enhanced oxygen migration process around the K dopant.

The smaller Li and Na dopants promote oxygen migration to a greater extent over the larger K and Rb dopants, which is the opposite of the trend seen for the oxygen vacancy formation energies. Doping with Li can promote unidirectional intra-layer oxygen migration, while Na doping can promote oxygen intra-layer migration in two directions. There is thus no correlation between the oxygen vacancy formation energies and the activation energies for the oxygen migration in the alkali metal doped bulk Chromia, as the origins of the enhanced reducibility and migration are based on the local properties of the particular dopant species which influence these processes in different ways. Since the oxygen migration pathways are complex in the alkali metal doped oxide, using the oxygen vacancy formation energy as a descriptor to predict the improvement in ionic conductivity for these systems is not possible. From our calculations, Na doping is the best promotor as the oxygen vacancy formation energy is low while it also has low activation energy barriers in both [010] and [100] directions for improving intra-layer ionic conductivity.

In understanding the effect of the dopants on oxygen migration, we note that work on oxygen vacancy migration in other oxides, e.g. ZrO_2, CeO_2 has implicated atomic relaxations around the vacancy in determining the migration barriers of the vacancy[92]. The strong relaxations around the defect site can act to impede migration of vacancies – the larger the relaxations then the less favourable is the migration process, with a larger barrier[92] and overcoming this can help to increase the ionic conductivity.

In the present work the magnitude of the relaxations around the vacancy site correlate with the ionic radius of the dopant – larger relaxations for a larger dopant. Thus if we consider migration along the (010) direction, as in figure 8, we note that the size of the largest barrier (which will determine the ionic conductivity) increases with an increase in the ionic radius of the dopant. Given that the magnitude of relaxations increases with the ionic radius of the dopant this finding appears to be consistent with the concept of large relaxations impeding the migration of vacancies [92] Thus a dopant in Cr_2O_3 such as Na may provide the best balance between ease of vacancy formation, atomic relaxations and lower migration barriers.

Modifying the oxygen vacancy migration process by alkali metal doing of Cr_2O_3 can improve the poison resistance of stainless steel (Cr-based) SOFC's and prevent Cr_2O_3 formation by inhibiting oxygen migration along the [110] direction due to the larger activation barriers as seen in this study.[20, 21, 23-25] The choice of alkali metal dopant can also be important as the dopant cations change isotropic diffusion in undoped Cr_2O_3 to anisotropic diffusion, which is a useful insight and an important property for next generation SOFC cathodes and electrolyte materials.[93, 94]

Table 4: The calculated rate limiting activation energies for the undoped and alkali metal doped bulk Chromia in each direction.

	[010] direction (eV)	[100] direction (eV)	[110] direction (eV)
Cr_2O_3	+3.30	+3.30	+3.30
Li-Cr_2O_3	+1.59	+3.14	+3.99
Na-Cr_2O_3	+2.83	+2.77	+4.41
K-Cr_2O_3	+3.04	+3.64	+3.06
Rb-Cr_2O_3	+4.52	+3.30	+4.34

Conclusions

The Density functional theory calculations using the Perdew-Burke-Ernzerhof (PBE) with the Hubbard +U correction (PBE+U) were used to investigate alkali metal (Li, Na, K, Rb) doping of bulk Chromium (III) oxide. Our calculations show that doping Chromia with these lower valence dopants results in hole formation on the lattice oxygen species which are compensated by formation of spontaneous oxygen vacancies. The removal of another oxygen atom termed 'the active oxygen vacancy' provides the formation energy relevant to experiment. Doping with alkali metals greatly improves the oxygen vacancy formation energy over the undoped Chromium oxide bulk with a correlation emerging between the oxygen vacancy formation energy and the ionic radius of the metal dopant; larger dopants (K, Rb) promote oxygen vacancy formation energy to a greater extent than smaller dopants (Li, Na).

The activation barriers for oxygen migration in the alkali metal doped Chromium bulk were also calculated to examine the effect of doping on the ionic conductivity. The calculated activation energies for undoped Chromia were found to be symmetric and isotropic. The presence of the dopants breaks this symmetry. Alkali dopants promote intra-layer oxygen migration in the {100} planes, while supressing inter-layer oxygen migration across the Cr cation layers. There were no observable correlations for the rate determining activation barriers of the doped bulk in each direction to either ionic size or oxygen vacancy formation energies. In contrast to the oxygen vacancy formation energies, the activation energies for oxygen migration can be lower for smaller ionic radius dopants (Li, Na) and are high for the larger ionic radius dopants (K, Rb). The smaller ionic dopants coupled with the position of the charge compensating oxygen vacancy, facilitate easier intra-layer ionic conductivity. The Na-Cr_2O_3 bulk strongly promotes both oxygen vacancy formation and migration, and can be a predicted novel candidate for electrolytes in medium temperature SOFCs, an alternative anode material to Li-Cr_2O_3,[20, 21] or as a promoter for oxygen evolution reactions,[14] and in high temperature methanol synthesis.[17]

Acknowledgements

We acknowledge support from the European Commission funded FP7-NMP project BIOGO (grant: 604296), the SFI/HEA funded Irish Centre for High-end Computing (ICHEC) and SFI funded local clusters at Tyndall, for computing resources. The COST ACTION CM1104 is also thanked for support.

References:

1. N. Popovici, M. L. Paramês, R. C. Da Silva, O. Monnereau, P. M. Sousa, A. J. Silvestre and O. Conde, *Applied Physics A: Materials Science and Processing*, 2004, 79, 1409-1411.
2. L. M. Corliss, J. M. Hastings, R. Nathans and G. Shirane, *Journal of Applied Physics*, 1965, 36, 1099-1100.
3. P. J. Brown, J. B. Forsyth, E. Lelièvre-Berna and F. Tasset, *Journal of Physics: Condensed Matter*, 2002, 14, 1957.
4. R. Zimmermann, P. Steiner and S. Hüfner, in *Proc. 11th Intern. Conf. Vac. UV Rad. Phys.* , eds. T. Miyahara, Y. Azuma, M. Watanabe and T. Ishii, Elsevier, Amsterdam, 1996, DOI: http://dx.doi.org/10.1016/B978-0-444-82245-1.50016-9, pp. 49-52.
5. T. Uozumi, K. Okada and A. Kotani, *Journal of Electron Spectroscopy and Related Phenomena*, 1996, 78, 103-106.
6. F. Lebreau, M. M. Islam, B. Diawara and P. Marcus, *The Journal of Physical Chemistry C*, 2014, 118, 18133-18145.
7. F. Maldonado, R. Rivera and A. Stashans, *Physica B: Condensed Matter*, 2012, 407, 1262-1267.
8. F. Maldonado, C. Novillo and A. Stashans, *Chemical Physics*, 2012, 393, 148-152.
9. A. Rohrbach, J. Hafner and G. Kresse, *Physical Review B*, 2004, 70, 125426.
10. Y. Guo, S. J. Clark and J. Robertson, *Journal of Physics: Condensed Matter*, 2012, 24, 325504.
11. G. Rollmann, A. Rohrbach, P. Entel and J. Hafner, *Physical Review B*, 2004, 69, 165107.
12. O. Nakayama, N. Ikenaga, T. Miyake, E. Yagasaki and T. Suzuki, *Industrial and Engineering Chemistry Research*, 2010, 49, 526-534.
13. S. A. El-Molla, *Applied Catalysis A: General*, 2005, 280, 189-197.
14. E. M. Calverley and K. J. Smith, *Industrial and Engineering Chemistry Research*, 1992, 31, 792-803.
15. J. A. Cline, A. A. Rigos and T. A. Arias, *The Journal of Physical Chemistry B*, 2000, 104, 6195-6201.
16. M. P. Brady, B. A. Pint, Z. G. Lu, J. H. Zhu, C. E. Milliken, E. D. Kreidler, L. Miller, T. R. Armstrong and L. R. Walker, *Oxidation of Metals*, 2006, 65, 237-261.
17. A. Beretta, Q. Sun, R. G. Herman and K. Klier, *Industrial and engineering chemistry research*, 1996, 35, 1534-1542.
18. S. Mehta, G. Simmons, K. Klier and R. Herman, *Journal of Catalysis*, 1979, 57, 339-360.
19. Ø. Borck and E. Schröder, *Journal of Physics: Condensed Matter*, 2006, 18, 10751.
20. R. F. Huang, A. K. Agarwal and H. U. Anderson, *Journal of the American Ceramic Society*, 1984, 67, 146-150.
21. J. Hu, H. Li, X. Huang and L. Chen, *Solid State Ionics*, 2006, 177, 2791-2799.
22. N. Kohli, O. Singh and R. Singh, *Applied Physics A*, 2012, 109, 585-590.
23. Y. Matsuzaki and I. Yasuda, *Journal of The Electrochemical Society*, 2001, 148, A126-A131.
24. X. Chen, P. Y. Hou, C. P. Jacobson, S. J. Visco and L. C. De Jonghe, *Solid State Ionics*, 2005, 176, 425-433.
25. Y. Liu and D. Chen, *international journal of hydrogen energy*, 2009, 34, 9220-9226.
26. M. Xiao, M. Zhao, X. Lang, Y. Zhu and Q. Jiang, *Chemical Physics Letters*, 2012, 542, 85-88.
27. M. Batzill, E. H. Morales and U. Diebold, *Physical review letters*, 2006, 96, 026103.
28. T. R. Gordon, M. Cargnello, T. Paik, F. Mangolini, R. T. Weber, P. Fornasiero and C. B. Murray, *Journal of the American Chemical Society*, 2012, 134, 6751-6761.
29. A. Iwaszuk and M. Nolan, *The Journal of Physical Chemistry C*, 2011, 115, 12995-13007.
30. A. Iwaszuk and M. Nolan, *Journal of Physics: Condensed Matter*, 2011, 23, 334207.

31. I. Nakamura, N. Negishi, S. Kutsuna, T. Ihara, S. Sugihara and K. Takeuchi, *Journal of Molecular Catalysis A: Chemical*, 2000, 161, 205-212.
32. R. Schaub, E. Wahlström, A. Rønnau, E. Lægsgaard, I. Stensgaard and F. Besenbacher, *Science*, 2003, 299, 377-379.
33. J. J. Carey and M. Nolan, *Applied Catalysis B: Environmental*, 2016, 197, 324-336.
34. J. J. Carey and M. Nolan, *Catalysis Science & Technology*, 2016, 6, 3544-3558.
35. P. Fornasiero, R. Dimonte, G. R. Rao, J. Kaspar, S. Meriani, A. Trovarelli and M. Graziani, *Journal of Catalysis*, 1995, 151, 168-177.
36. P. R. Keating, D. O. Scanlon and G. W. Watson, *Chemical Physics Letters*, 2014, 608, 239-243.
37. P. R. Keating, D. O. Scanlon and G. W. Watson, *Journal of Materials Chemistry C*, 2013, 1, 1093-1098.
38. P. R. Keating, D. O. Scanlon, B. J. Morgan, N. M. Galea and G. W. Watson, *The Journal of Physical Chemistry C*, 2012, 116, 2443-2452.
39. A. B. Kehoe, D. O. Scanlon and G. W. Watson, *Chemistry of Materials*, 2011, 23, 4464-4468.
40. M. Nolan, *The Journal of Physical Chemistry C*, 2011, 115, 6671-6681.
41. R. Gerhardt-Anderson and A. Nowick, *Solid State Ionics*, 1981, 5, 547-550.
42. X. Aparicio-Anglès, A. Roldan and N. H. de Leeuw, *Chemistry of Materials*, 2015, 27, 7910-7917.
43. P. Qin, G. Fang, Q. He, N. Sun, X. Fan, Q. Zheng, F. Chen, J. Wan and X. Zhao, *Solar Energy Materials and Solar Cells*, 2011, 95, 1005-1010.
44. P. Qin, G. Fang, N. Sun, X. Fan, Q. Zheng, F. Chen, J. Wan and X. Zhao, *Thin Solid Films*, 2011, 519, 4334-4341.
45. H. Cao, X. Qiu, Y. Liang, M. Zhao and Q. Zhu, *Applied Physics Letters*, 2006, 88, 241112.
46. S.-Y. Choi, M.-H. Kim and Y.-U. Kwon, *Physical Chemistry Chemical Physics*, 2012, 14, 3576-3582.
47. E. Arca, K. Fleischer, S. A. Krasnikov and I. Shvets, *The Journal of Physical Chemistry C*, 2013, 117, 21901-21907.
48. I. Ayub, F. J. Berry, C. Johnson, D. A. Johnson, E. A. Moore, X. Ren and H. M. Widatallah, *Solid State Communications*, 2002, 123, 141-145.
49. A. Holt and P. Kofstad, *Solid State Ionics*, 1997, 100, 201-209.
50. J. S. Park and H. G. Kim, *Journal of the American Ceramic Society*, 1988, 71, 173-176.
51. M. Wojciechowska, I. Tomska-Foralewska, W. Przystajko and M. Zieliński, *Catalysis Letters*, 2005, 104, 121-128.
52. J. Pan, U. V. Waghmare, N. Kumar, C. O. Ehi-Eromosele and C. N. R. Rao, *ChemPhysChem*, 2015, 16, 1502-1508.
53. A. B. Kehoe, A. Elisabetta, D. O. Scanlon, I. V. Shvets and G. W. Watson, *Journal of Physics: Condensed Matter*, 2016, 28, 125501.
54. E. Arca, K. Fleischer and I. V. Shvets, *Applied Physics Letters*, 2011, 99, 111910.
55. J. J. Carey, M. Legesse and M. Nolan, *The Journal of Physical Chemistry C*, 2016, 120, 19160-19174.
56. S. Goel, A. Kumar, J. K. Quamara and J. Kumar, *Advanced Science Letters*, 2014, 20, 1562-1566.
57. M. Nolan, *Journal of Materials Chemistry*, 2011, 21, 9160-9168.
58. K. J. W. Atkinson, R. W. Grimes, M. R. Levy, Z. L. Coull and T. English, *Journal of the European Ceramic Society*, 2003, 23, 3059-3070.
59. C. R. A. Catlow, J. Corish, J. Hennessy and W. C. Mackrodt, *Journal of the American Ceramic Society*, 1988, 71, 42-49.
60. T. Horita, K. Yamaji, Y. Xiong, H. Kishimoto, N. Sakai and H. Yokokawa, *Solid State Ionics*, 2004, 175, 157-163.
61. J. Vaari, *Solid State Ionics*, 2015, 270, 10-17.
62. A. C. S. Sabioni, B. Lesage, A. M. Huntz, J. C. Pivin and C. Monty, *Philosophical Magazine A*, 1992, 66, 333-350.
63. A. C. S. Sabioni, A. M. Huntz, F. Millot and C. Monty, *Philosophical Magazine A*, 1992, 66, 351-360.
64. A. C. S. Sabioni, A. M. Huntz, F. Millot and C. Monty, *Philosophical Magazine A*, 1992, 66, 361-374.
65. M. Nolan, J. E. Fearon and G. W. Watson, *Solid State Ionics*, 2006, 177, 3069-3074.
66. D. A. Andersson, S. I. Simak, N. V. Skorodumova, I. A. Abrikosov and B. Johansson, *Proceedings of the National Academy of Sciences of the United States of America*, 2006, 103, 3518-3521.
67. C. Frayret, A. Villesuzanne, M. Pouchard and S. Matar, *International Journal of Quantum Chemistry*, 2005, 101, 826-839.
68. R. A. De Souza, A. Ramadan and S. Horner, *Energy & Environmental Science*, 2012, 5, 5445-5453.
69. P. P. Dholabhai, J. B. Adams, P. Crozier and R. Sharma, *The Journal of Chemical Physics*, 2010, 132, 094104.
70. S. Kobi, N. Jaiswal, D. Kumar and O. Parkash, *Journal of Alloys and Compounds*, 2016, 658, 513-519.
71. D. S. Aidhy, *Physical Chemistry Chemical Physics*, 2016, 18, 15019-15024.
72. J. P. Perdew and W. Yue, *Physical review B*, 1986, 33, 8800.
73. J. P. Perdew, K. Burke and M. Ernzerhof, *Physical review letters*, 1996, 77, 3865.
74. G. Kresse and J. Furthmüller, *Computational Materials Science*, 1996, 6, 15-50.
75. G. Kresse and J. Furthmüller, *Physical Review B*, 1996, 54, 11169.
76. G. Kresse and J. Furthmüller, *Phys. Rev. B*, 1996, 54, 169.
77. G. Kresse and J. Hafner, *Journal of Physics: Condensed Matter*, 1994, 6, 8245.
78. G. Kresse and D. Joubert, *Physical Review B*, 1999, 59, 1758.
79. S. L. Dudarev, A. I. Liechtenstein, M. R. Castell, G. A. D. Briggs and A. P. Sutton, *Physical Review B*, 1997, 56, 4900-4908.
80. S. Dudarev, G. Botton, S. Savrasov, C. Humphreys and A. Sutton, *Physical Review B*, 1998, 57, 1505.
81. B. J. Morgan and G. W. Watson, *Physical Review B*, 2009, 80, 233102.
82. H. J. Monkhorst and J. D. Pack, *Physical Review B*, 1976, 13, 5188.
83. F. Murnaghan, *Proceedings of the national academy of sciences of the United States of America*, 1944, 30, 244.
84. R. K. Di Cerbo and A. U. Seybolt, *Journal of the American Ceramic Society*, 1959, 42, 430-431.
85. G. Henkelman, A. Arnaldsson and H. Jónsson, *Computational Materials Science*, 2006, 36, 354-360.
86. E. Sanville, S. D. Kenny, R. Smith and G. Henkelman, *Journal of computational chemistry*, 2007, 28, 899-908.
87. W. Tang, E. Sanville and G. Henkelman, *Journal of Physics: Condensed Matter*, 2009, 21, 084204.

88. G. Henkelman, B. P. Uberuaga and H. Jónsson, *The Journal of chemical physics*, 2000, 113, 9901-9904.
89. G. Henkelman, G. Jóhannesson and H. Jónsson, in *Theoretical Methods in Condensed Phase Chemistry*, Springer, 2002, pp. 269-302.
90. D. Sheppard, R. Terrell and G. Henkelman, *The Journal of chemical physics*, 2008, 128, 134106.
91. N. K. McGuire and M. O'Keeffe, *Journal of Solid State Chemistry*, 1984, 54, 49-53.
92. D. Marrocchelli, S. R. Bishop and J. A. Kilner, *J. Mater. Chem.*, 2013, 1, 7673-7680.
93. A. Chroneos, B. Yildiz, A. Tarancón, D. Parfitt and J. A. Kilner, *Energy & Environmental Science*, 2011, 4, 2774-2789.
94. M. n. Burriel, J. Peña-Martínez, R. J. Chater, S. Fearn, A. V. Berenov, S. J. Skinner and J. A. Kilner, *Chemistry of Materials*, 2012, 24, 613-621.

